

# A functional series time-dependent framework for non-stationary modeling and statistical damage diagnosis via ultrasonic guided waves

Shabbir Ahmed<sup>1</sup>  and Fotis Kopsaftopoulos<sup>2</sup> 

## Abstract

This study presents a novel statistical structural damage diagnosis framework using ultrasonic guided wave signals. The approach employs functional series time-dependent autoregressive (FS-TAR) models to capture the non-stationary dynamics of guided wave propagation. Unlike traditional methods that analyze only initial wave packets, this framework utilizes complete guided wave signals, including reflected waves, providing a comprehensive assessment of structural state. The FS-TAR model represents time-varying parameters through deterministic evolution using orthogonal basis functions. Three basis function families, namely, wavelet, Chebyshev, and trigonometric, have been evaluated to determine optimal signal representation. The covariance structure of the estimated time-invariant coefficients of projection vector and time-varying model parameters is extensively investigated, and their role in damage diagnosis is assessed. Two complementary damage diagnosis approaches are developed: one based on time-invariant projection coefficients and another using time-dependent model parameters. Both approaches employ statistical hypothesis testing with established confidence bounds derived from the asymptotic properties of the parameter estimators. Experimental validation is conducted on an aluminum plate under various damage scenarios, including both damage-intersecting and non-intersecting wave propagation paths. Results demonstrate accurate and robust damage detection and classification across all tested states. The wavelet basis functions show superior performance, providing the clearest parameter separation between healthy and damaged states. Key advantages include (i) utilization of complete wave signals rather than isolated wave packets, (ii) response-only operation without requiring input measurements, (iii) established statistical framework with quantified uncertainties, and (iv) real-time applicability with minimal computational requirements.

## Keywords

Guided waves, stress waves, time series models, damage diagnosis, non-stationarity, autoregressive model, coda waves, FS-TAR, wavelet basis, uncertainty quantification

## Introduction

Guided waves can be generated within thin structural components and used for diagnosing damage within a structure.<sup>1</sup> These waves, due to their short wavelengths, are sensitive to small defects within structural components and have the potential to monitor large areas of complex structures in an automated fashion.<sup>2–5</sup> The widespread adoption of guided wave-based damage diagnosis techniques is facilitated by their simple generation and detection from the surface of the structure with the help of piezoelectric, usually Lead Zirconate Titanate (PZT), transducers.<sup>2,6</sup> PZT transducers are low-cost, lightweight, can be mounted to the structure permanently in large quantities, are unobtrusive to the

structure, and offer the possibility of real-time monitoring of structures.<sup>7–9</sup> The fundamental premise is that the damage within a structure such as cracks, corrosion, dents, debonding, delamination, etc., introduces wave scattering and induces changes in the waveform.

<sup>1</sup>Department of Mechanical Engineering, South Dakota State University, Brookings, SD, USA

<sup>2</sup>Department of Mechanical, Aerospace and Nuclear Engineering, Rensselaer Polytechnic Institute, Troy, NY, USA

### Corresponding author:

Fotis Kopsaftopoulos, Department of Mechanical, Aerospace and Nuclear Engineering, Rensselaer Polytechnic Institute, 110 8th Street, Troy, NY 12180-3522, USA.  
Email: [kopsaf@rpi.edu](mailto:kopsaf@rpi.edu)

These changes are manifested as alterations in guided wave amplitude, time of flight, wave packet shape, and the emergence of new wave packets due to additional reflections and scattering introduced by damage. The concept of fault indicators or damage indices (DIs) emerges from expressing and modeling these changes in the guided wave signals.<sup>8,10,11</sup>

In the case of time-domain DI formulations, usually the symmetric  $S_0$  and/or anti-symmetric  $A_0$  mode wave packets are considered in the diagnostic phase.<sup>11–16</sup> The reflection portion of the signals is often neglected as it may complicate the signal processing and diagnostic approach while it may mask specific damage signatures. The reflection or the trailing portion of the signal, which occurs after the first arrival wave packets (depending on the geometry, usually after the  $S_0$  and  $A_0$  modes), may be also referred to as the coda wave.<sup>17–19</sup> Coda wave analysis techniques (typically known as coda wave interferometry), such as the doublet and stretching methods have been proposed to detect weak changes or micro-cracks in solid materials. It should be noted that coda wave interferometry heavily relies on the trailing part of the signal and has been applied in the context of damage detection for concrete and composite structures.<sup>17,20</sup> To increase the damage detection capability, frequency-domain or time-frequency-domain (mixed-domain) DIs were introduced.<sup>21–23</sup> Nonlinear features such as higher-order harmonics extracted from ultrasonic waves have been used to formulate DIs that can detect micro-scale fatigue cracks.<sup>24</sup> An entropy-based method for monitoring minor changes in structures was proposed in Ibáñez et al.,<sup>25</sup> Rojas et al.<sup>26</sup> Although the majority of traditional DI-based damage diagnosis methods are deterministic, recently, several probabilistic and/or statistical methods have been proposed to formulate DIs that can also represent uncertainties.<sup>9,27,28</sup> Gaussian mixture models and Gaussian process regression models are examples of such formulations. Probability density functions for the DI of different structural states are formulated and compared, instead of using a single value. Several other DI formulations can be found in references.<sup>29–32</sup> However, when incorporating the reflection portion of the signals (coda waves), these types of methods may show suboptimal performance.<sup>27</sup> Recently, a nonlinear autoregressive network with exogenous input (NARX) model has been proposed for damage diagnosis of structures using guided waves.<sup>33,34</sup> The method requires limited training data and shows promise in damage detection and localization, particularly when the multi-step-ahead prediction scheme is utilized. A Gaussian process NARX model has also been proposed for defect diagnosis in anisotropic structural components.<sup>35</sup> The NARX model structure may offer an unnecessarily complex and elaborate solution to the

wave modeling challenge, as simpler model structures have been shown to provide accurate and robust results.<sup>36,37</sup> Simpler time-dependent autoregressive (TAR) model structures can model time-varying guided wave signals, potentially offering additional knowledge about their time-dependent frequency content, thus capturing the wave propagation characteristics and physics of the system. Guided waves are narrowband non-stationary (time-varying) signals, as their statistical properties depend on time.<sup>38,39</sup> To accurately represent the non-stationarity of these signals, time-varying time series models can be employed.

Stochastic time-varying time series models have been previously used where the excitation is a low frequency (usually less than 1000 Hz) random white (Gaussian) noise, and as a consequence the low-frequency vibrating modes of the structure are excited.<sup>40–47</sup> Interested readers can consult references<sup>48–51</sup> where both stationary and non-stationary time series models were utilized in the context of low-frequency random vibration-based damage diagnosis. On the other hand, ultrasonic guided waves are the result of high-frequency vibrations in plate-like structures and contain information about the high-frequency (ultrasonic) dynamics of the structural system.<sup>52</sup> High-frequency broadband random excitation and its response were analyzed in Ahmed and Kopsaftopoulos<sup>53</sup> using functionally pooled models. The modeling of time-varying responses is a challenging problem, which requires detailed analysis and the use of appropriate models.<sup>54–56</sup>

The identification process for time-dependent time series involves mathematical models that utilize stochastic ordinary difference equations representing the underlying structural dynamics. Non-parametric identification methods may include time or frequency domain approaches, and are easier to use compared to parametric methods.<sup>54</sup> However, non-parametric methods may suffer from lower accuracy and time-frequency representation capability due to the conflicting requirements needed for time and frequency resolution.

Parametric methods provide superior modeling accuracy in terms of representation capability and frequency resolution.<sup>49,54,57</sup> Recently, parametric models were used to tackle vibration-based damage diagnosis of non-stationary structures.<sup>49,50</sup> The methods are based on statistical decision-making via likelihood ratio tests employing functional series time-dependent autoregressive with exogenous excitation model residuals. This model type requires the availability of both input and output signals. However, measurements of the excitation signals may be unavailable, and damage diagnosis using a response-only representation might be preferred, that is, functional series time-dependent autoregressive (FS-TAR) models (that do not use input signals).

FS-TAR representations are identified and implemented in this study for developing a statistical damage diagnosis (detection and classification) scheme utilizing guided wave signals. The proposed method relies on response-only (output-only) guided wave signals. The method employs the complete wave propagation signals, including the reflection portion (coda wave), thus relaxing the requirement of traditional DI-based methods to use only the first wave packets (symmetric and anti-symmetric modes). The method is capable of achieving accurate and robust modeling of ultrasonic waves via FS-TAR models that consider the deterministic evolution of time-varying parameters for a specific structural geometry. Three early preliminary studies on this topic were previously published.<sup>36,37,51</sup>

In the present study, a rigorous, complete, and detailed analysis and assessment are presented with appropriate mathematical formulations. The notable advantages of using FS-TAR models for damage diagnosis may be described as: (i) damage diagnosis is not based on identifying changes in specific wave packets, such as the  $S_0$  and  $A_0$  modes. The majority of the proposed active-sensing detection and localization methods utilize this approach. Additionally, the separation between the  $S_0$  and  $A_0$  modes may not be distinct due to boundary effects or anisotropy, and the automation effort to separate the two modes may be difficult. The FS-TAR-based approach is free of such limitations. (ii) The FS-TAR-based framework is material agnostic, that is, the same method can be applied to different structural systems, sensor configurations, and materials such as metals and composites irrespective of the specific mode wave propagation characteristics. (iii) The FS-TAR-based method may offer insight into the dispersive nature of the guided wave's frequency content and the uncertainty or noise levels in the received signals, thus allowing for interpretable results and physical insight.<sup>49,50</sup> Time series models, such as autoregressive (AR), autoregressive moving average (ARMA), autoregressive with exogenous excitation (ARX), time-varying autoregressive (TAR), etc., originate from the system identification, times series analysis, and modal analysis communities, offering clear physical interpretability compared to traditional maximum likelihood (ML) approaches. Specifically, the time-dependent parameters of a TAR model constitute the denominator of the system's time-varying transfer function, which directly connects to the system's discrete-time poles. Each pole inherently represents a pair of natural frequency and damping ratio of the system, thereby establishing a direct and physically meaningful link to the fundamental dynamics governing the system. Compared to traditional ML methods, which often operate in a black box configuration, time series models explicitly incorporate system dynamics and

causal relationships. This explicit structure enables direct interpretation of parameter changes over time. Consequently, time series models provide valuable insights into the physical mechanisms driving observed behaviors, facilitating informed and transparent decision-making. Traditional machine learning architectures, such as artificial neural networks (ANNs), have the potential to effectively model both stationary and non-stationary signals. However, they typically lack interpretability from a physics-based perspective. The parameters (weights) of ANNs generally do not possess explicit physical meanings and cannot be directly linked to underlying structural dynamics or specific wave propagation characteristics. Consequently, despite their potential predictive capability, such machine learning models often fall short in providing insights into the physical processes driving the observed phenomena.

In the case of the FS-TAR model representation, the time-dependent parameters are projected onto properly selected subspaces spanned by orthogonal basis functions. The selection of the basis functions is guided by the representation parsimony principle and prior knowledge of the associated physics. The basis functions that have been utilized in the literature include time-varying polynomial functions,<sup>58</sup> orthogonal polynomial basis functions such as Chebyshev<sup>59</sup> and Legendre<sup>60</sup> polynomials, trigonometric basis functions,<sup>61</sup> discrete prolate spheroidal functions,<sup>62</sup> various wavelet families, and others.<sup>63</sup> Although these orthogonal basis functions constrain the progression of the non-stationary model parameters in a predetermined way, the choice of a specific functional subspace may be arbitrary. In this regard, in the present study, three different families of basis functions are investigated and critically assessed, namely, the wavelet, Chebyshev, and trigonometric basis functions. The novel contributing aspects of this study can be outlined as follows:

- Complete experimental evaluation of FS-TAR model-based damage diagnosis for guided ultrasonic wave-based structural health monitoring (SHM).
- Use of complete available guided wave propagation signals, that is, the first arrival wave packets (the  $S_0$  and  $A_0$  modes) as well as the coda waves (the reflections portion), rather than relying only on the  $S_0$  and  $A_0$  modes.
- Exploration and assessment of the associated structural dynamics modeling using wavelet, Chebyshev, and trigonometric functional subspaces.
- Extraction of model parameter confidence bounds through the use of estimator asymptotic properties and probability distributions. Formulation of time-invariant and time-varying statistical quantities and probabilistic thresholds.

To summarize, section “Stochastic FS-TAR modeling of guided waves” outlines the modeling and evaluation of guided wave propagation using the FS-TAR model and the associated model identification scheme. Section “Damage diagnosis via functional series models” presents the functional series-based fault detection framework. The theory behind a statistical damage diagnosis scheme based on time-invariant coefficients of projection (COP) and time-dependent model parameters is presented. Section “Experimental investigation and results” describes the experimental setup, data acquisition process, and obtained results. Section “Discussion” provides a thorough discussion of the obtained results and their implications. Finally, section “Conclusion” provides a synopsis of the study and suggests avenues for future work.

## Stochastic FS-TAR modeling of guided waves

Ultrasonic guided waves, a type of Lamb waves propagating on thin-walled structures, exhibit time-dependent characteristics, necessitating the use of time-varying models for their representation and analysis.<sup>54,64,65</sup> FS-TAR models are used in this study to model guided wave signals. Section “Deterministic parameter evolution models” outlines the wave representation via functional series time-dependent autoregressive (FS-TAR) models. Sections “COP estimation” and “FS-TAR model identification” present the parameter estimation and model identification processes. Section “Model validation” explains how to validate an identified model.

### Deterministic parameter evolution models

A non-stationary TAR model can be represented by the following stochastic difference equation:

$$y[t] + \sum_{i=1}^{na} a_i[t] \cdot y[t-i] = e[t], \text{ with } e[t] \sim \text{iid } \mathcal{N}(0, \sigma_e^2[t]) \quad (1)$$

Note that the signal value  $y$  at time  $t$  ( $y[t]$ ) is dependent on its previous  $na$  time steps plus a random noise term  $e[t]$ . The noise term  $e[t]$  is Gaussian and independently and identically distributed (iid) with time-varying standard deviation  $\sigma_e[t]$ . The TAR model parameters  $a_i[t]$  also depend upon time.

Under the FS-TAR formulation, the model parameters  $a_i[t]$  evolve in a deterministic way, and a specific structure is imposed on them rather than allowing them to evolve in a stochastic or random manner. This is accomplished by projecting the time-dependent model

parameters onto properly selected deterministic functional subspaces. Thus, the AR parameters and residual standard deviation are projected onto the chosen orthogonal basis functions, as follows:

$$\mathcal{F}_{AR} \triangleq \{G_{b_a(1)}[t], G_{b_a(2)}[t] \dots G_{b_a(p_a)}[t]\} \quad (2)$$

$$\mathcal{F}_{\sigma_e} \triangleq \{G_{b_s(1)}[t], G_{b_s(2)}[t] \dots G_{b_s(p_s)}[t]\} \quad (3)$$

In the above equations,  $\mathcal{F}$  designates a subspace that contains the orthogonal basis functions  $G_j[t]$ .  $p_a$  and  $p_s$  represent the AR and standard deviation subspace dimensionalities, respectively.  $b_a(i)(i=1, \dots, p_a)$  and  $b_s(i)(i=1, \dots, p_s)$  designate the indices of the particular orthogonal basis functions. The time-dependent AR and innovations standard deviation of an FS-TAR( $na$ )<sub>[ $p_a, p_s$ ]</sub> representation may be expressed as:

$$a_i[t] \triangleq \sum_{j=1}^{p_a} a_{i,j} \cdot G_{b_a(j)}[t], \sigma_e[t] \triangleq \sum_{j=1}^{p_s} s_j \cdot G_{b_s(j)}[t] \quad (4)$$

The parameters  $a_{i,j}$  and  $s_j$  are referred to as the COP for the AR and innovations or residual standard deviation, respectively. Consequently, the projection coefficients  $a_{i,j}$  and  $s_j$  are the essence of the FS-TAR model. It is noteworthy that at any given time  $t$ , the time-varying AR model parameters  $a_i[t]$  are obtained by scalar multiplication of  $a_{i,j}$  and  $G_{b_a(j)}[t]$ . Since there are no quadratic or higher-order terms included, these models are linear-in-the-parameter models.

### COP estimation

The COP vectors  $\boldsymbol{\vartheta}$  and  $\mathbf{s}$  of the FS-TAR model are defined as follows:

$$\boldsymbol{\vartheta} \triangleq [a_{1,1} \ a_{1,2} \ \dots \ a_{1,pa} : \dots : a_{na,1} \ a_{na,2} \ \dots \ a_{na,pa}]^T_{(na \times pa) \times 1} \quad (5)$$

$$\mathbf{s} \triangleq [s_1 \ s_2 \ \dots \ s_{ps}]^T_{ps \times 1} \quad (6)$$

By combining equations (1) and (4), the FS-TAR model can be expressed in the following way:

$$y[t] + \sum_{i=1}^{na} \sum_{j=1}^{pa} a_{i,j} \cdot G_{b_a(j)}[t] \cdot y[t-i] = e[t, \boldsymbol{\vartheta}] \quad (7)$$

The backshift operator  $\mathcal{B}$  (also referred to as the lag operator) operates on an element of a time series to yield the preceding element as follows:

$$\mathcal{B} \cdot y[t] \triangleq y[t-1]; \mathcal{B}^2 \cdot y[t] \triangleq y[t-2]; \mathcal{B}^i \cdot y[t] \triangleq y[t-i] \quad (8)$$

In terms of the backshift operator, equation (7) can be expressed as:

$$y[t] + \sum_{i=1}^{na} \sum_{j=1}^{pa} a_{i,j} \cdot G_{b_a(j)}[t] \cdot \mathcal{B}^i \cdot y[t] = e[t, \boldsymbol{\vartheta}] \quad (9)$$

which can be rearranged as:

$$\left( 1 + \sum_{i=1}^{na} \sum_{j=1}^{pa} a_{i,j} \cdot G_{b_a(j)}[t] \cdot \mathcal{B}^i \right) \cdot y[t] = e[t, \boldsymbol{\vartheta}] \quad (10)$$

The introduced backshift operator is a fundamental tool in time series modeling allowing concise and intuitive representations of temporal dependencies by shifting a time series backward by one or more time steps. It simplifies the formulation of time series models, providing clear algebraic structures for both theoretical analysis and practical identification procedures. Additionally, it simplifies the derivation of invertibility and stationarity states.<sup>65</sup> For instance, if all roots of the characteristic polynomial associated with the backshift operator lie outside the unit circle, the process is stationary. Moreover, employing linear regression forms facilitates the estimation of model parameters and their confidence intervals, providing clear computational advantages. A linear regression form can be obtained from equation (7) as follows:

$$y[t] = \boldsymbol{\phi}_A^T[t] \cdot \boldsymbol{\vartheta} + e[t, \boldsymbol{\vartheta}] \quad (11)$$

with

$$\boldsymbol{\phi}_A^T[t] \triangleq [-G_{b_a(1)}[t] \cdot y[t-1], \dots, -G_{b_a(pa)}[t] \cdot y[t-na]]_{(na-pa) \times 1}^T \quad (12)$$

A prediction error (PE) criterion can be formed to estimate the unknown vector  $\boldsymbol{\vartheta}$  as follows

$$\hat{\boldsymbol{\vartheta}} = \arg \min_{\boldsymbol{\vartheta}} \sum_{t=1}^N e^2[t, \boldsymbol{\vartheta}] \quad (13)$$

Here,  $\arg \min$  refers to the optimization process in which the sum of squares of the PE has to be minimized in order to estimate the unknown vector  $\boldsymbol{\vartheta}$ . The minimization leads to the formulation of the ordinary least squares (OLSSs) estimator:

$$\hat{\boldsymbol{\vartheta}}^{OLS} = \left( \frac{1}{N} \cdot \sum_{t=1}^N \boldsymbol{\phi}_A[t] \cdot \boldsymbol{\phi}_A^T[t] \right)^{-1} \cdot \left( \frac{1}{N} \cdot \sum_{t=1}^N \boldsymbol{\phi}_A[t] \cdot y[t] \right) \quad (14)$$

While the OLSSs estimator can yield biased estimates and lack asymptotic efficiency, the maximum likelihood (ML) estimator offers unbiased, consistent, and

asymptotically efficient estimates. The ML estimation of the COP vector  $\boldsymbol{\vartheta}$  may be obtained through the maximization of the log-likelihood function, which for the FS-TAR model and under the Gaussian assumption for the innovations sequence may be given as:

$$\ln \mathcal{L}(\boldsymbol{\vartheta}, \boldsymbol{\sigma}_e | y^N) = -\frac{N}{2} \ln 2\pi - \frac{1}{2} \sum_{t=1}^N \left( \ln \sigma_e^2[t] + \frac{e^2[t, \boldsymbol{\vartheta}]}{\sigma_e^2[t]} \right) \quad (15)$$

$$\hat{\boldsymbol{\vartheta}}^{ML} = \arg \max_{\boldsymbol{\vartheta}} \{ \ln \mathcal{L}(\boldsymbol{\vartheta}, \boldsymbol{\sigma}_e | y^N) \} = \arg \max_{\boldsymbol{\vartheta}} \left[ -\frac{1}{2} \sum_{t=1}^N \ln e^2[t, \boldsymbol{\vartheta}] \right] \quad (16)$$

with  $\hat{\sigma}_e^2[t] = e^2[t, \hat{\boldsymbol{\vartheta}}]$ . The estimation of  $e[t, \hat{\boldsymbol{\vartheta}}]$  is obtained by using a moving average filter realized through a sliding time window. The innovations' standard deviation COP vector  $\boldsymbol{s}$  may be obtained as follows:

$$\hat{\sigma}_e[t] = \sum_{j=1}^{ps} s_j \cdot G_{b_s(j)}[t] = \mathbf{g}^T[t] \cdot \boldsymbol{s} \quad (17)$$

where

$$\mathbf{g}[t] \triangleq [G_{b_s(1)}[t], G_{b_s(2)}[t], \dots, G_{b_s(ps)}[t]]_{ps \times 1}^T \quad (18)$$

$$\hat{\boldsymbol{s}}^{ML} = \arg \min_{\boldsymbol{s}} \left\{ -\frac{1}{2} \sum_{t=1}^N \left( \ln (\mathbf{g}^T[t] \cdot \boldsymbol{s})^2 \right) + \frac{e^2[t, \hat{\boldsymbol{\vartheta}}]}{(\mathbf{g}^T[t] \cdot \boldsymbol{s})^2} \right\} \quad (19)$$

The ML estimation of  $\boldsymbol{s}$  involves a non-linear optimization process. The constraint  $\mathbf{g}^T[t] \cdot \boldsymbol{s} > 0$  is imposed during the optimization process to ensure numerical stability. One important aspect of this estimation process is that the theoretical covariance matrix of the projection vector  $\boldsymbol{\vartheta}$  is available and can be obtained as<sup>49</sup>:

$$P_{\boldsymbol{\vartheta}} = \frac{1}{N} \cdot \left\{ \frac{1}{N} \sum_{t=1}^N \frac{\boldsymbol{\phi}_A[t] \cdot \boldsymbol{\phi}_A^T[t]}{(\mathbf{g}_s^T[t] \cdot \hat{\boldsymbol{s}}^{ML})^2} \right\}^{-1} \cdot \left\{ \frac{1}{N} \sum_{t=1}^N \frac{\sigma_e^2[t] \cdot \boldsymbol{\phi}_A[t] \cdot \boldsymbol{\phi}_A^T[t]}{(\mathbf{g}_s^T[t] \cdot \hat{\boldsymbol{s}}^{ML})^4} \right\} \cdot \left\{ \frac{1}{N} \sum_{t=1}^N \frac{\boldsymbol{\phi}_A[t] \cdot \boldsymbol{\phi}_A^T[t]}{(\mathbf{g}_s^T[t] \cdot \hat{\boldsymbol{s}}^{ML})^2} \right\}^{-1} \quad (20)$$

This covariance matrix satisfies the fundamental statistical bound known as the Cramer-Rao lower bound. Note that  $P_{\boldsymbol{\vartheta}}$  is not a function of time. In this work, the covariance matrix obtained from equation (20) is referred to as the “theoretical covariance” or “FS-TAR-based covariance.”

The FS-TAR parameter vector  $\boldsymbol{\theta}[t] = [a_1[t], a_2[t], \dots, a_{na}[t]]$  and the associated covariance matrix  $P[t]$  are time-dependent. In the present study, during the collection of the experimental data, at least 20 trials or

realizations of ultrasonic signals were collected. After performing FS-TAR modeling of the ultrasonic signals, the 20 realizations yield a set of 20 COP vectors. A covariance matrix can be obtained from this set of 20 COP vectors. In the work, this approach of obtaining the sample covariance matrix is referred to as the “experimental or sample covariance of the COP vector.” Similarly, the 20 realizations yield a set of 20 time-dependent model parameters. The covariance matrix obtained from these 20 realizations of time-varying parameters is referred to as the “experimental or sample covariance of the time-dependent model parameters.”

### FS-TAR model identification

The FS-TAR model identification involves determining the AR order  $na$ , the functional subspaces  $\mathcal{F}_{AR}$ ,  $\mathcal{F}_{\sigma_e}$ , their respective dimensionalities ( $pa$  and  $ps$ ), and the indices for the basis functions. The model identification can be accomplished via either a heuristic or evolutionary algorithm-based optimization scheme. In this study, two types of search schemes were utilized to identify candidate model structures. The first is an evolutionary optimization method based on genetic algorithms (GAs) while the second is based on a heuristic or suboptimal scheme. Different candidate basis function families such as polynomial, trigonometric, wavelet, etc. are predetermined. When an infinite number of basis functions are utilized, any orthogonal basis functions can approximate a given function with arbitrary accuracy. In this regard, the choice of the orthogonal basis function is arbitrary.

In general, an *integer optimization scheme* consists of two distinct phases. In the initial phase of the optimization process, promising regions within the search space where the optimal model structures may exist are identified. The process aims at maximizing the negative Akaike information criterion (AIC)<sup>66</sup> or Bayesian information criterion (BIC).<sup>67</sup> In the second phase, further refinement of the outcomes of the first phase to pinpoint the globally optimal structure is performed. Starting from maximum argument values, it iteratively reduces either the AR order  $na$  or one of the subspace dimensionalities ( $pa, ps$ ) until the decrease in AIC or BIC values assumes a constant value. Finally, the model structure that provides the minimum AIC or BIC is chosen. In addition to AIC or BIC criteria, the residual sum of squares (RSS) over the signal sum of squares (SSS) value (designated as RSS/SSS) can be also used as a fitness criterion.

**Model structure selection via a GA-based approach.** The GA-based scheme enables comprehensive searches and

offers significant automation benefits. It relies solely on the AIC or BIC criteria. When implementing a GA, the user needs to provide upper and lower bounds for the  $na$ ,  $pa$ , and  $ps$  ranges. For example, typical bounds for the guided waves modeling could be  $na \in [2, 8]$ ,  $pa \in [1, 10]$ , and  $ba \in [1, 10]$ . Once these bounds are provided, the GA will perform the optimization for  $na$ ,  $pa$ , and  $ps$  simultaneously, searching for the global minimum based on the BIC criterion. The GA begins by randomly generating an initial set of individuals within the provided bounds, where each individual represents a specific combination of parameters  $[na, pa, ps]$ . In order to implement the key features of the GAs, such as crossover and mutation, the  $na$ ,  $pa$ , and  $ps$  values are encoded in the form of binary digits. For example, an individual may have a binary representation such as  $na = [011]$ ,  $ba = [10110]$ ,  $bs = [011]$ , which can be compactly expressed as a vector  $[na, ba, bs] = [0110110011]$ . A group of such encoded individuals is referred to as a “population”, the size of which can vary depending on the complexity of the problem. Once a population is established, the algorithm performs crossover (mating) by randomly selecting pairs of individuals from the population and exchanging portions of their binary strings. To maintain genetic diversity and introduce new variations, mutation is applied at a predefined probability, flipping individual bits from 0 to 1 or from 1 to 0. This iterative process continues until convergence criteria are met. Although this scheme offers the possibility of exhaustive searches and is fully automated, it is exclusively based upon the fitness function (usually the AIC/BIC criteria) and may lead to over parameterization, which may affect the damage diagnosis performance. Furthermore, domain knowledge is important for appropriately defining the bounds of  $na$ ,  $pa$ , and  $ps$ . For a more detailed and comprehensive explanation, readers are referred to references.<sup>54,68</sup> Compared to the GA approach, heuristic methods involve less automation and are inherently more subjective, requiring greater expert intervention and judgment.

**Model structure selection via a heuristic approach.** The key idea for the *heuristic or suboptimal search scheme* is to separate the model structure selection problem into two smaller subproblems: (i) the model order  $na$  selection subproblem and (ii) the functional subspaces ( $pa, ps, b_a(j), b_s(j)$ ) selection subproblem. This is achieved by fixing one set of parameters and optimizing the other in order to minimize the interaction between the two subproblems. In the first phase of the heuristic search scheme, an extended and complete (including consecutive basis functions) set of functional subspaces is initially considered and kept constant for all

candidate model orders  $na$ . The AR order yielding the minimum AIC or BIC is then chosen for the subsequent phase of selecting the final basis functions. However, with limited data, this approach may encounter estimation challenges due to a low sample per parameter (SPP) values.

Next, the selected AR order  $na$  is kept fixed, and the redundant functional subspaces are sequentially removed without significantly reducing model accuracy. While this scheme may not yield the globally optimal structure, it proves effective in practice due to its straightforward implementation, reduced computational complexity, and adaptability. Compared to the GA-based approach, the heuristic scheme has reduced automation potential, is subjective to a higher degree, and expert intervention is needed.

### Model validation

Model validation is a crucial step in the modeling process, as it helps to assess the validity of the model's underlying assumptions and the model's capability to capture the true behavior of the structural system. The validation process involves formal validation procedures typically based upon the posterior examination of the underlying assumptions, such as the model's residual series uncorrelatedness (whiteness) and Gaussianity. In the case of non-stationary models, such as in the case of FS-TAR models, the residual whiteness or uncorrelatedness test may not be suitable due to the time-dependent variance of the residuals. To address this issue, the residual sign test or runs test (MATLAB function `runstest.m`) can be applied. This test searches for the sequence of positive or negative sign fluctuations in the residual series, which can provide insights into the uncorrelatedness of the residuals.<sup>54</sup> A long sequence of the same sign in the residual implies that there are dynamics present in the signal that have not been captured. This phenomenon may lead to acceptance of the alternative hypothesis of the runs test, and therefore, the validation may fail. Additional challenges may arise when a short transient signal is being modeled. Once a model has been identified and the COP vector has been estimated, the damage diagnosis process can be implemented as discussed in the next section (section "Damage diagnosis via functional series models").

### Damage diagnosis via functional series models

In this study, the FS-TAR non-stationary modeling framework is utilized for both representing ultrasonic

guided wave signals and developing two subsequent damage diagnosis methods.

To perform the proposed FS-TAR-based damage diagnosis scheme, the discretized response (output) wave signals  $y[t]$ , indexed from  $t=1$  to  $N$ , from different structural states are denoted with subscripts  $(o, a, b, \dots, u)$ , where  $o$  represents for nominal (healthy) state and  $u$  the unknown potentially damaged states. The subscripts  $a, b, \dots$  represent different damage states. Typically, raw experimental signals undergo preprocessing steps such as signal down-sampling, normalization, or filtering. The preprocessed guided wave signals are then modeled and analyzed using the non-stationary FS-TAR modeling approach. An appropriate model structure is identified, as presented in the previous sections, and applied to data collected during both baseline and inspection phases. Model parameters are estimated based on the identified model structure using specific datasets from each phase. Characteristic quantities, denoted as  $Q$  or  $Q[t]$ , are subsequently derived from either the estimated time-invariant COP or the time-varying model parameters, respectively.

Damage detection is performed by comparing the true values of  $Q_u$  (or  $Q_u[t]$ ) with those of  $Q_o$  (or  $Q_o[t]$ ) using statistical hypothesis testing. Similarly, damage identification involves comparing  $Q_u$  (or  $Q_u[t]$ ) with each of  $Q_a, Q_b, \dots$  (or  $Q_a[t], Q_b[t], \dots$ ) through statistical hypothesis testing procedures. The complete process of damage diagnosis using FS-TAR models is shown in Figure 1.

### Time-invariant projection coefficient-based method

In this section, a statistical damage diagnosis scheme is proposed based on the use of vector  $\boldsymbol{\vartheta}$  that contains the time-invariant COP  $a_{i,j}$  which can be obtained from the available non-stationary guided wave signals after selecting a specific model structure. The estimated COP vector is designated as  $\hat{\boldsymbol{\vartheta}}$  and can be obtained via different estimators, such as the maximum likelihood (ML), OLSs, and weighted least squares (WLSs; see section "COP estimation"). In this work, ML estimators have been used for their unbiased and asymptotically efficient properties. For a sufficiently long wave signal, the ML estimator asymptotically follows a normal distribution with mean the true, but unknown, vector  $\boldsymbol{\vartheta}$  and covariance matrix  $\mathbf{P}_{\boldsymbol{\vartheta}}$ , that is:

$$\hat{\boldsymbol{\vartheta}} \sim \mathcal{N}(\boldsymbol{\vartheta}, \mathbf{P}_{\boldsymbol{\vartheta}}) \quad (21)$$

The damage detection problem involves examining statistically significant changes in vector  $\boldsymbol{\vartheta}$ . This process requires a formal hypothesis testing procedure between the estimated parameters of the nominal and current, that is, unknown, structural state. If the statistical

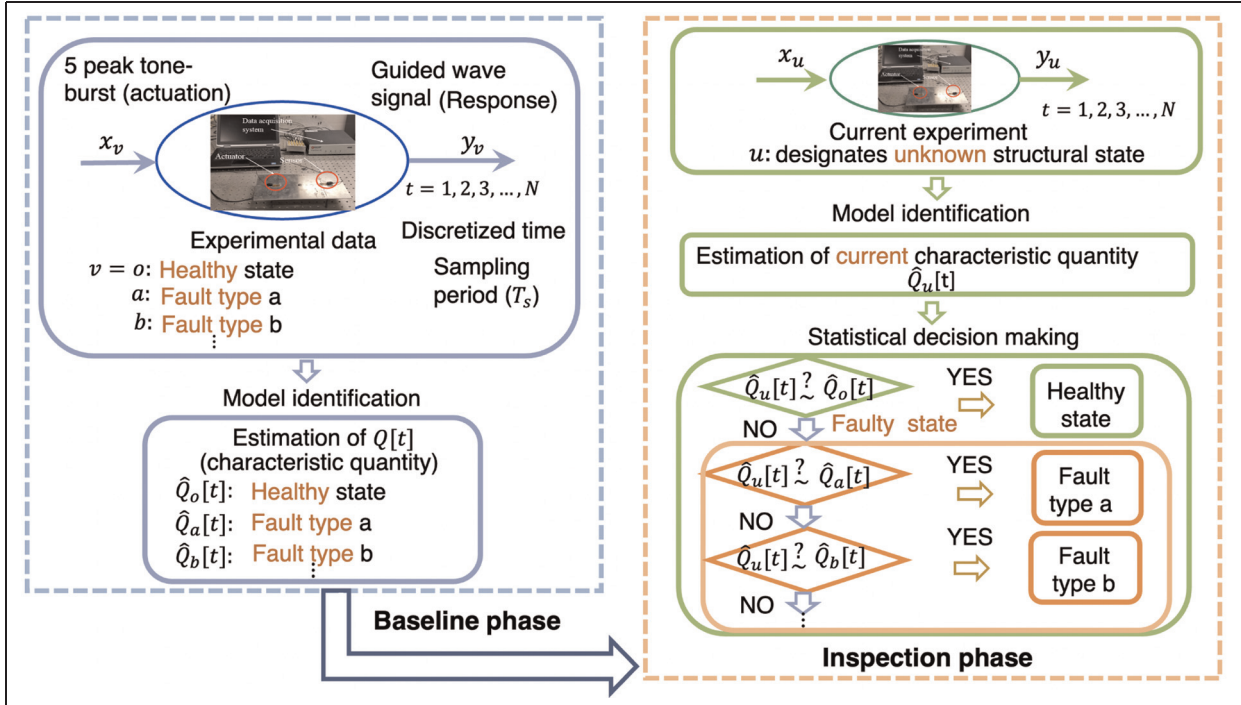


**Figure 1.** Complete methodology for non-stationary FS-TAR model-based damage diagnosis algorithm for ultrasonic guided wave-based SHM.

SHM: structural health monitoring.

difference between the nominal  $\boldsymbol{\vartheta}_o$  and  $\boldsymbol{\vartheta}_u$  is zero, then the structure is determined to be in a healthy state, and this forms the null hypothesis  $H_0$  (healthy structure). If the difference is statistically significant, then the structure is declared damaged, and the alternative hypothesis  $H_1$  (damaged structure) prevails. The difference  $\delta\hat{\boldsymbol{\vartheta}}$  is assumed normally distributed ( $\delta\hat{\boldsymbol{\vartheta}} = \hat{\boldsymbol{\vartheta}}_o - \hat{\boldsymbol{\vartheta}}_u \sim \mathcal{N}(0, 2\mathbf{P}_o)$ ) and a characteristic quantity  $Q$  is formulated as follows:

$$Q = \delta\hat{\boldsymbol{\vartheta}}^T \cdot \delta\mathbf{P}^{-1} \cdot \delta\hat{\boldsymbol{\vartheta}} \text{ with } \delta\mathbf{P} = 2\mathbf{P}_o \quad (22)$$

As the true covariance matrix  $\mathbf{P}_o$  corresponding to the nominal healthy structural state is unknown, its estimated counterpart  $\hat{\mathbf{P}}_o$  is used. However, the probability distribution of the statistical quantity  $Q$  depends on the type of estimated covariance matrix used: (i) theoretical based on the asymptotic distribution of the model parameters given by equation (20) or (ii) sample covariance matrix obtained from the estimated FS-TAR models and corresponding parameter vectors when multiple data sets are available. The test statistic  $Q$  follows a  $\chi^2$  distribution with  $d$  degrees of freedom that correspond to the dimension of the parameter vector  $\boldsymbol{\vartheta}$ . If the computed  $Q$  is less than the probabilistic threshold  $\chi^2_{1-\alpha}(d)$ , the structure is considered healthy at an  $\alpha$  (type I) error probability level.

In order to tackle the damage identification task, similar hypothesis tests may be formulated between the COP vector  $\hat{\boldsymbol{\vartheta}}_u$  of the current structural state and those corresponding to potential damage states  $\hat{\boldsymbol{\vartheta}}_A, \hat{\boldsymbol{\vartheta}}_B, \dots$

#### Time-dependent model parameter-based method

In this method, damage diagnosis is based on a time-dependent characteristic quantity  $Q[t] = f(\boldsymbol{\theta}[t])$ , which is a function of the FS-TAR time-varying parameter vector  $\boldsymbol{\theta}[t] \triangleq [a_1[t] \ a_2[t] \ \dots \ a_{na}[t]]_{na \times 1}^T$  that can be obtained from equation (4).

The time-dependent parameter vector  $\hat{\boldsymbol{\theta}}[t]$  represents an estimate of the true parameter vector  $\boldsymbol{\theta}[t]$ . At each time instant,  $\hat{\boldsymbol{\theta}}[t]$  follows a Gaussian distribution with true mean  $\boldsymbol{\theta}[t]$  and corresponding time-varying covariance matrix  $\mathbf{P}[t]$ . The estimation process for the time-varying covariance matrix  $\hat{\mathbf{P}}[t]$  is described in detail in section “COP estimation.” Therefore,

$$\hat{\boldsymbol{\theta}}[t] \sim \mathcal{N}(\boldsymbol{\theta}[t], \mathbf{P}[t]) \quad (23)$$

To perform damage diagnosis using time-dependent parameters, a hypothesis testing procedure is conducted at each time instant. When the difference  $\boldsymbol{\theta}_o[t] - \boldsymbol{\theta}_u[t] = 0$  between the time-dependent parameter vectors is statistically zero  $\boldsymbol{\theta}_o[t] - \boldsymbol{\theta}_u[t] = 0$ , the null hypothesis at

every time instant ( $H_0[t]$ ) prevails, and the structure is determined to be in its healthy state. In the opposite case, where the difference  $\theta_o[t] - \theta_u[t] \neq 0$  is statistically significant at a time instant  $t$ , the alternative hypothesis ( $H_1[t]$ ) is selected at the  $\alpha$  (type I) risk level.

Damage identification utilizing time-varying parameters relies on similar multiple hypothesis testing problems at each time instant. The parameter vector  $\hat{\theta}_u[t]$ , estimated under the current structural state, is statistically compared via hypothesis tests to the vectors estimated under the considered damage types  $\hat{\theta}_A[t], \dots, \hat{\theta}_B[t]$ .

## Experimental investigation and results

### Experiments and guided wave data generation

For consistency and comparison purposes, this study employs the identical aluminum coupon and dataset as in previous research.<sup>36,37</sup> Compared to the prior works, the present study offers a thorough analysis and critical experimental assessment of the proposed FS-TAR-based damage diagnosis methods. A 6061 aluminum plate with dimensions  $11 \times 6 \times 0.093$  inches was mounted on a tensile testing machine (Instron, Inc.). Six PZT piezoelectric transducers were positioned on the plate surface, as depicted in Figure 2(b), for generating and receiving guided wave signals. The disc-shaped PZTs, acquired from Acellent Technologies, Inc., have a diameter of 1/4 inch and a thickness of 0.0079 inch. Small steel weights (3 g each, up to four weights) were gradually added to the plate with adhesive tapes to simulate local damage in the form of increased effective stiffness and wave scattering generation. The specific configurations of the plate with added weights are referred to as “structural states,” leading to four distinct damage levels (dams 1–4). At each state, 20 guided wave signals were collected from each wave propagation path. Guided waves were generated using 5-peak tone burst (Hamming-windowed sine wave) actuation signals with a center frequency of 250 kHz and recorded at 24 MHz sampling frequency. A ScanGenie III (Acellent Technologies, Inc.) data acquisition system was used to generate and receive the guided wave signals. The collected data were post-processed and down-sampled to 2 MHz, resulting in  $N = 612$  sample-long signals. An illustrative signal realization for different structural states and path is shown in Figure 2(c). The scattered signals and non-parametric spectrograms are depicted in Figure 3(a) and (c), respectively.

Figure 2(c) depicts representative ultrasonic guided wave signals for two distinct path (damage intersecting path 2–6 and damage non-intersecting path 1–4) for different damage levels (top and middle subplots). The

bottom subplot shows the comparison of the signals for these path under the nominal structural state. Figure 3(a) presents the corresponding scatter signals for damage levels 1 and 3, and path 2–6 and 1–4. Figure 3(b) shows the dispersion curve of the 6061 aluminum plate with 2.36 mm thickness.<sup>5</sup> From the dispersion curve, it can be observed that for a 250 kHz actuation frequency, only the  $S_0$  and  $A_0$  modes can be excited within the plate. Additionally, the  $S_0$  mode has higher phase velocity than the  $A_0$  mode. It should also be noted that in the bottom subplot of Figure 2(c) there is a distinct time delay between the two signals for path 2–6 and 1–4 of about 1  $\mu$ s (see Figure 2(b) for the distance between path 2–6 and 1–4). This experimental time delay matches the theoretical predictions from the dispersion curve in Figure 3(b). To evaluate the proposed FS-TAR-based damage diagnosis approach against a conventional time-domain DI, the DI formulation from Janapati et al.<sup>11</sup> was employed. The DI results are presented in detail in Ahmed and Kopsaftopoulos.<sup>7</sup>

### Model identification from experimental guided wave data

In this study, FS-TAR models are employed to represent non-stationary guided wave signals that propagate in a deterministic way within a thin-walled plate structure.<sup>69</sup> Three types of functional subspaces are considered, namely: (i) wavelet basis functions, (ii) Chebyshev basis functions, and (iii) trigonometric basis functions.

Since we assumed the  $\mathcal{F}_{AR}$  and  $\mathcal{F}_{\sigma_e}$  to be preselected, we have to determine the model order  $na$ , the functional subspace dimension, and the exact basis function indices in order to obtain the FS-TAR model that best represents the wave propagation for the employed paths. To accomplish this, initially we employed the heuristic model structure selection approach in which the BIC was evaluated for a sequence of  $na$  AR orders and an initially large number of basis functions. In the present case, for all three functional subspaces, model orders from  $na=2$  to  $na=10$  were considered. For each order  $na$ ,  $pa=10$  and  $ps=10$  were selected to define the initial functional subspaces. Once an appropriate model order  $na$  was selected,  $na$  and  $ps$  terms were kept fixed, and the AR functional basis dimensionality was consecutively varied from  $pa=1$  to  $pa=10$ . The same methodology was adopted for determining the appropriate  $ps$  value and their indices.<sup>49,54</sup>

Figure 4 presents indicative FS-TAR model identification results based on the heuristic method for the case of wavelet basis functions and damage intersecting path 2–6. A similar approach was adopted for Chebyshev and trigonometric basis functions for the

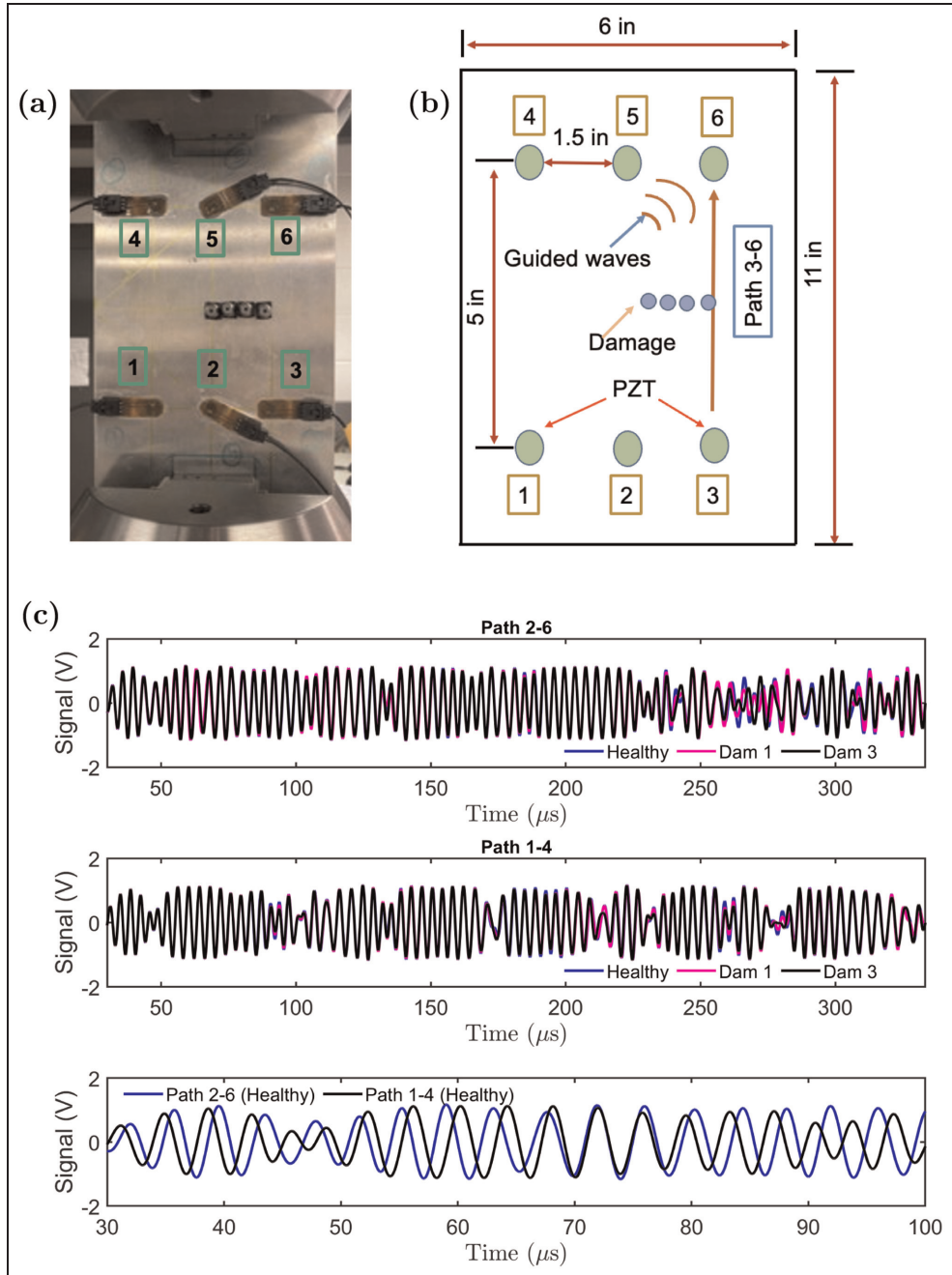


**Figure 2.** (a) The experimental coupon mounted on the tensile testing machine with no applied load; (b) the schematic of the sensor placement and major dimensions of the plate; and (c) representative guided ultrasonic wave signals for both nominal and damaged scenarios (damage level 1 and damage level 3): damage intersecting path 2–6 (top subplot), damage non-intersecting path 1–4 (middle subplot), and the time delay between the signals from path 2–6 and path 1–4.

two path considered. Figure 4(a) depicts the RSS/SSS evolution with increasing model order  $na$ . The RSS/SSS value sharply drops when  $na=4$ , and then reaches a plateau for higher model orders. Figure 4(b) shows the BIC versus model order  $na$ . The BIC monotonically decreases as the model order increases. A higher model order may provide lower BIC and RSS/SSS

values, but at the same time may create artifacts and lead to overfitting. Consequently,  $na=4$  was chosen as the optimal FS-TAR model order. Figure 4(c) presents the BIC values with increasing AR basis dimensionality  $pa$ , set model order  $na=4$ , and set innovations standard deviation basis dimensionality  $ps$ . It should be noted that the BIC value is minimum when the first

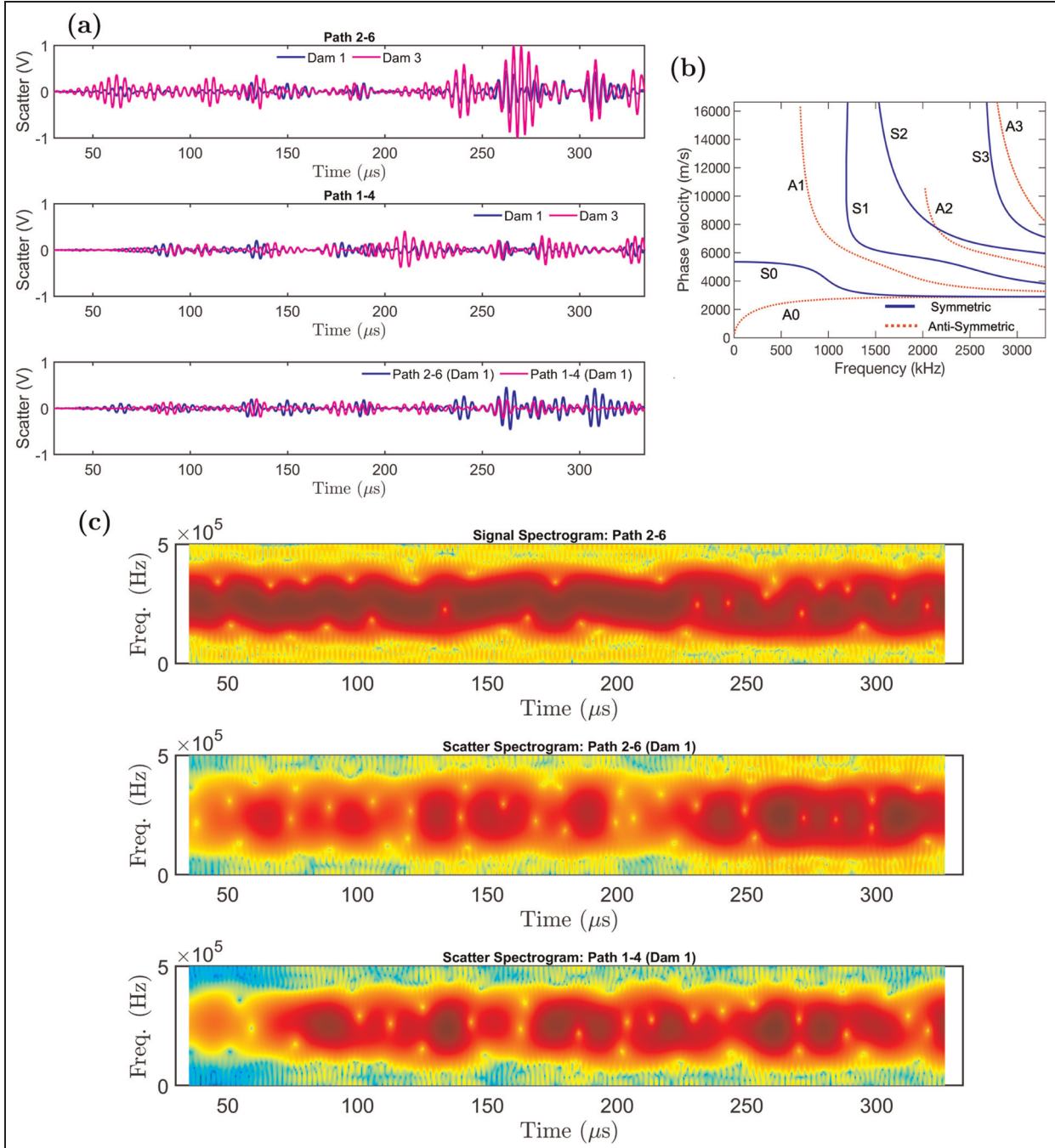


**Figure 3.** (a) Scatter signal comparison for the two path studied in this paper: path 2–6 (damage intersecting) and path 1–4 (damage non-intersecting); (b) the dispersion curve for the 6061 aluminum with 2.36 mm thickness; (c) representative spectrograms for the guided wave signals (top subplot) and scatter signals (middle and bottom subplots).

eight consecutive basis functions are used. However, choosing the first eight consecutive basis functions reduces the SPP value and tends to cause overfitting. As a result, only the first four consecutive basis functions were used. For similar reasons and from Figure 4(d), which shows the BIC versus the innovation standard

deviation basis dimensionality  $ps$ , only the first two consecutive basis functions were used. Note that the above-mentioned model order selection process is suboptimal and follows the heuristic approached of section “FS-TAR model identification.” It should also be noted that it requires a certain degree of user expertise.

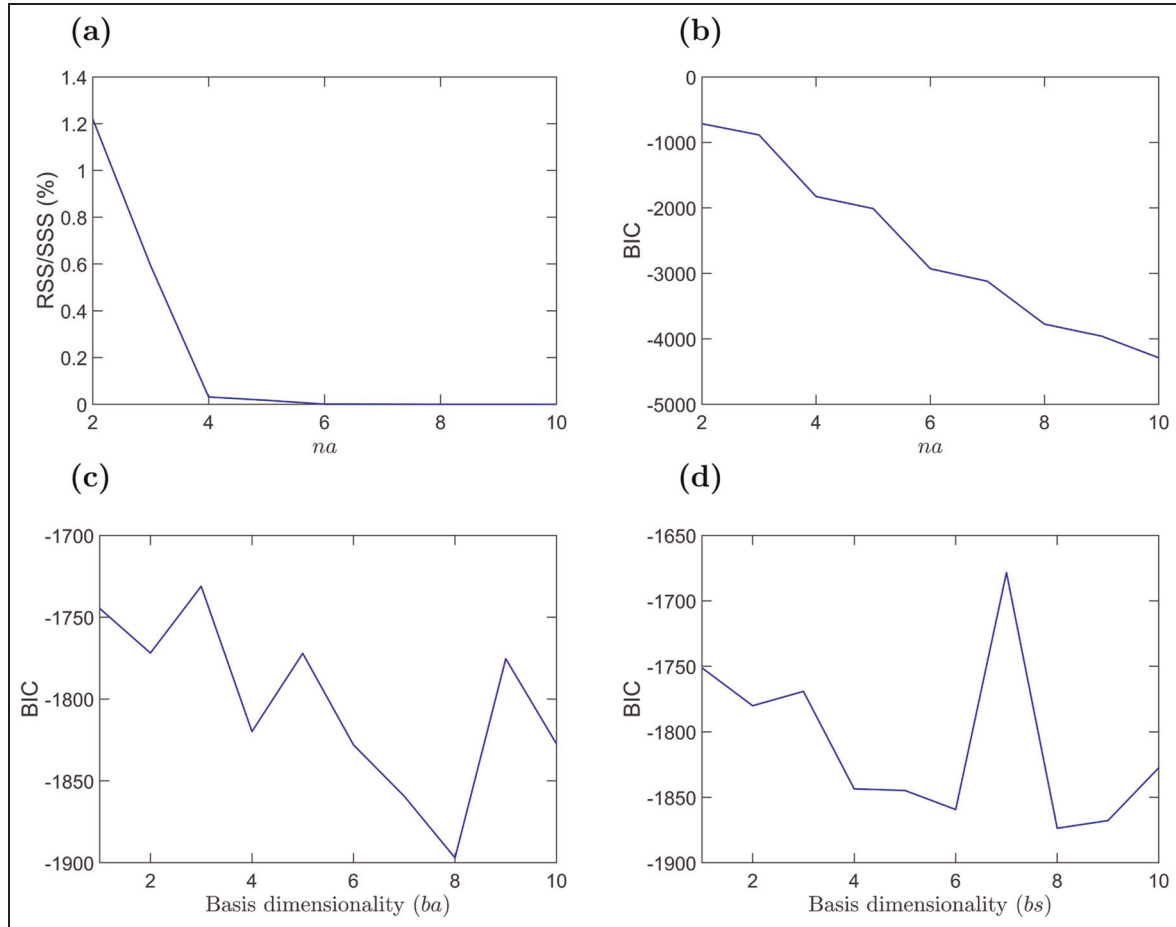


**Figure 4.** FS-TAR model identification for the guided wave signal received from the aluminum structure for damage intersecting path 2–6 using wavelet basis functions: (a) RSS/SSS versus the model order  $na$  with the first 10 consecutive AR and innovations standard deviation wavelet basis functions; (b) BIC versus model order  $na$  with the first ten consecutive AR and innovations standard deviation wavelet basis functions; (c) BIC versus AR basis function dimensionality ( $ba$ ) with model order  $na=4$  and the first ten consecutive innovations standard deviation wavelet basis functions; (d) BIC versus innovations standard deviation basis function dimensionality ( $bs$ ) with model order  $na=4$  and the first 10 consecutive AR wavelet basis functions.

In addition to using the heuristic model structure selection method, the GA-based integer optimization scheme was also utilized for selecting the appropriate model structure. The GA-based optimization method suggests that a model order  $na=4$  with the functional subspaces  $\mathcal{F}_{AR}=\{G_1[t], G_2[t], G_3[t], G_4[t]\}$  ( $pa=4$ ) and  $\mathcal{F}_{\sigma_e}=\{G_1[t], G_2[t]\}$  ( $ps=2$ ) should be used as the optimal model structure (for path 2–6). Thus, the identified model structure is FS-TAR(4)<sub>[4,2]</sub>. A similar procedure was followed to identify the model structure for path 1–4 ( $na=4$  and  $\mathcal{F}_{AR}=\{G_1[t], G_2[t], G_3[t], G_4[t], G_5[t]\}$  ( $pa=5$ ) and  $\mathcal{F}_{\sigma_e}=\{G_1[t], G_2[t], G_3[t]\}$  ( $ps=3$ )). Thus, the identified model structure is FS-TAR(4)<sub>[5,3]</sub>. The identified model structures for Chebyshev and trigonometric basis functions for damage intersecting and non-intersecting path are summarized in Table 1.

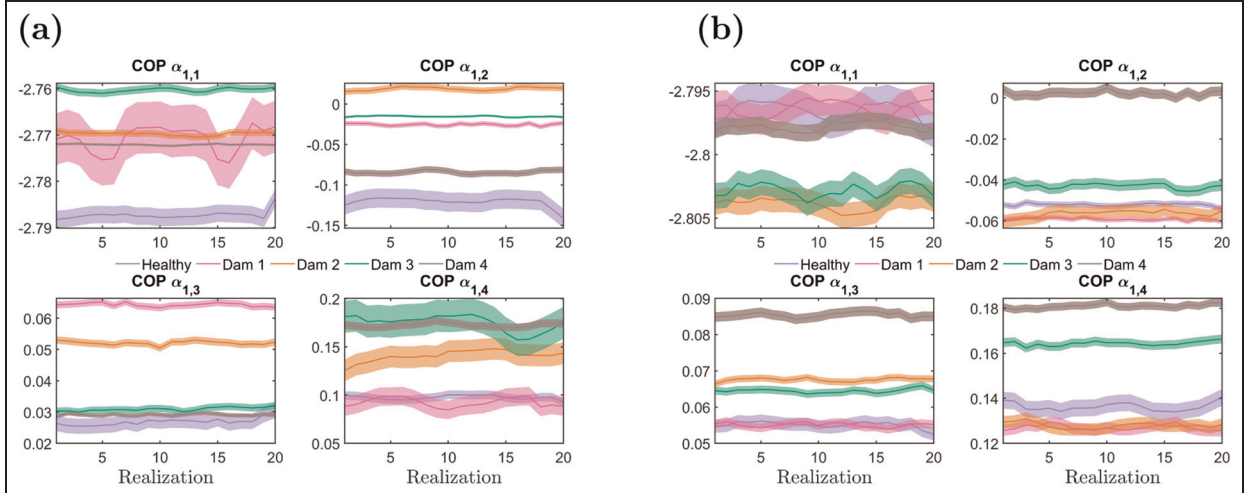
Model parameter estimation was achieved via the asymptotically efficient maximum likelihood (ML) estimator. Different estimators, such as OLS or WLS would yield slightly different parameter estimates and asymptotic parameter distribution, consequently influencing the subsequent damage diagnosis process.

#### Investigation of model parameters and confidence intervals

In this section, the estimated model parameter spaces and the associated confidence intervals are presented and assessed with respect to the considered structural (healthy and damage) states. The objective is to provide a critical insight into the models' representation capability for the different structural states and to

**Table 1.** Compact representation of the identified basis functions and the indices for different cases.

Basis function	Path	AR basis indices	$\sigma_e$ indices	Identified model
Wavelet basis	1–4	$\{G_1[t], G_2[t], G_3[t]\}$ $\{G_4[t], G_5[t]\} (pa=5)$	$\{G_1[t], G_2[t]\}$ $\{G_3[t]\} (ps=3)$	FS-TAR(4) <sub>[5, 3]</sub>
	2–6	$\{G_1[t], G_2[t]\}$ $\{G_3[t], G_4[t]\} (pa=4)$	$\{G_1[t], G_2[t]\} (ps=2)$	FS-TAR(4) <sub>[4, 2]</sub>
Chebyshev basis	1–4	$\{G_1[t], G_8[t]\} (pa=2)$	$\{G_1[t], G_2[t]\}$ $\{G_3[t]\} (Ps=3)$	FS-TAR(4) <sub>[2, 3]</sub>
	2–6	$\{G_1[t], G_3[t]\}$ $\{G_6[t]\} (pa=3)$	$\{G_1[t], G_4[t]\}$ $\{G_5[t]\} (ps=3)$	FS-TAR(4) <sub>[3, 3]</sub>
Trigonometric basis	1–4	$\{G_1[t], G_3[t]\}$ $\{G_4[t], G_9[t]\} (pa=4)$	$\{G_1[t], G_2[t]\}$ $\{G_4[t]\} (ps=3)$	FS-TAR(4) <sub>[4, 3]</sub>
	2–6	$\{G_1[t], G_6[t]\}$ $\{G_8[t]\} (pa=3)$	$\{G_1[t], G_2[t]\}$ $\{G_3[t]\} (ps=3)$	FS-TAR(4) <sub>[3, 3]</sub>

**Figure 5.** The COP values for various structural states of the coupon under investigation, estimated using wavelet orthogonal basis functions: the mean COP values are shown as thick lines, while the shaded portions indicate the corresponding  $\pm 2$  standard deviations. (a): path 2–6 and (b): path 1–4.

investigate potential patterns and significant differences that can facilitate or hinder the damage diagnosis tasks.

Figure 5(a) and (b) showcases the first four AR, COP values utilizing the wavelet basis functions. Various structural states: nominal and damage levels from 1 to 4 are shown for path 2–6 and path 1–4. From Table 1, it can be noted that for wavelet orthogonal basis functions and path 2–6, there are 16 AR COPs ( $na \cdot pa = 4 \cdot 4 = 16$ ). The first four AR COPs, namely,  $\alpha_{1,1}, \alpha_{1,2}, \alpha_{1,3}, \alpha_{1,4}$ , are shown to visualize their evolution for different structural states. For each structural state, 20 samples are shown. The  $\pm 2$  standard deviation confidence bounds depicted as shaded portions were obtained from 20 experimental signal realizations. In Figure 5(a) (damage intersecting path 2–6), the separation between COPs of different structural states,

particularly for  $\alpha_{1,2}$ , is noticeable, with narrower confidence intervals compared to  $\alpha_{1,1}, \alpha_{1,3}, \alpha_{1,4}$ . For COP  $\alpha_{1,3}$ , damage level 4 overlaps with the healthy case (baseline). For COP  $\alpha_{1,4}$ , damage level 3 shows the largest deviation from the healthy case. On the other hand, in Figure 5(b), the COPs have overlapped across various states (with some exceptions). Similar observations can be made for Chebyshev and trigonometric orthogonal basis functions. The better the separation among the COPs of different structural states, the better the performance of the FS-TAR scheme. As a result, damage non-intersecting path are more challenging for damage detection due to the higher degree of overlapping of the COP values among various structural states.

Figure 6(a) and (b) shows the progression of COP  $\alpha_{1,1}$  across five structural states. Results from both

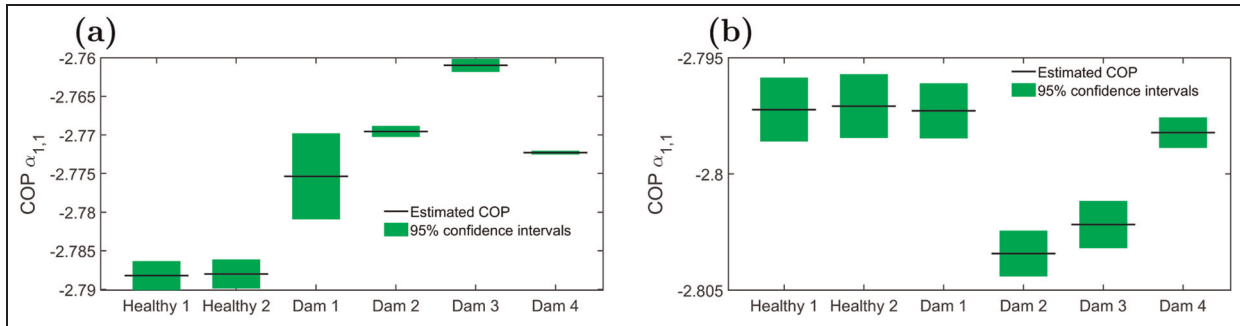


**Figure 6.** Indicative estimates of coefficients of projection (COP) for both nominal and damaged states, along with the corresponding 95% confidence intervals: (a) showcases COP  $\alpha_{1,1}$  for path 2–6 (damage intersecting path) using wavelet basis functions, while (b) shows the same for path 1–4 (damage non-intersecting path). Note that the standard deviation is higher for the COPs from path 1–4.

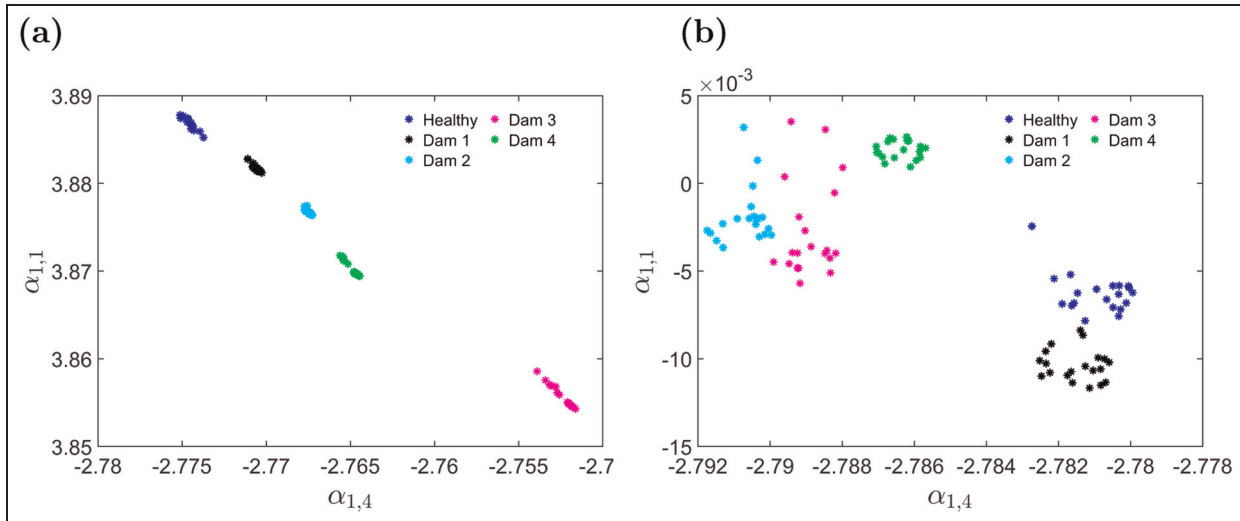


**Figure 7.** Correlation between the COP  $\alpha_{1,1}$  versus COP  $\alpha_{1,4}$  using Chebyshev orthogonal basis functions: (a) for path 2–6; (b) for path 1–4. The COPs exhibit a closer clustering pattern for path 2–6 (damage intersecting path). COP: coefficients of projection.

path 2–6 and path 1–4 are shown. Wavelet basis functions were used as the orthogonal basis functions. The mean parameter values are depicted by the black lines, and the green shades denote the  $\pm 2$  standard deviations. Distinct structural states are discernible for COPs from path 2–6 (Figure 6(a)), with no overlapping in confidence intervals, except for damage level 1, whose confidence interval is notably wider than the other states. Figure 6(b) illustrates the COPs from path 1–4. It should be noted that the confidence bounds for damage levels 1 and 4 overlap with the healthy cases. Similar trends can be observed for other COPs as well, which are not presented here for conciseness.

Figure 7(a) and (b) depicts the clustering patterns among the COPs obtained under different structural

states. The correlation between the COP  $\alpha_{1,1}$  and COP  $\alpha_{1,4}$  is presented for path 2–6 and 1–4, respectively. Chebyshev orthogonal basis functions are used in this case. The COPs are tightly clustered for damage intersecting path 2–6, while they are more dispersed or loosely clustered for damage non-intersecting path 1–4. Similar observations can be made when using wavelet and trigonometric orthogonal basis functions.

Figure 8(a) and (b) shows the three-dimensional view of the correlation among the COP  $\alpha_{1,1}$ ,  $\alpha_{1,2}$ , and  $\alpha_{1,4}$  for different path using Chebyshev orthogonal basis functions. Note that the COPs for the same structural states are closely clustered and non-overlapping for damage intersecting path 2–6, while the opposite is true for path 1–4.

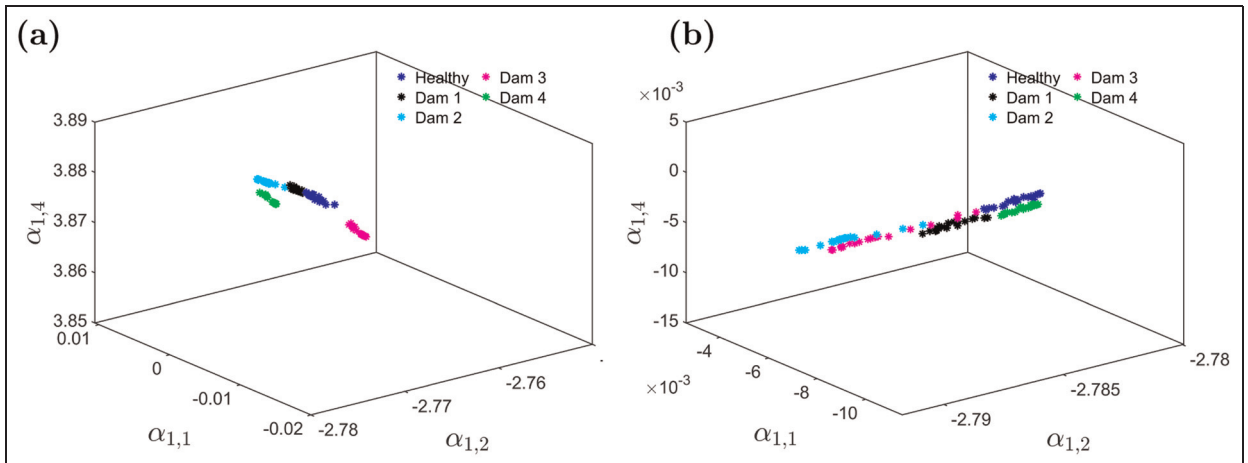


**Figure 8.** Correlation between the COP  $\alpha_{1,1}$ , COP  $\alpha_{1,2}$  and COP  $\alpha_{1,4}$  in a three-dimensional visualization (Chebyshev orthogonal basis functions): (a) path 2–6, (b) path 1–4. As observed in the two-dimensional scenario, the COPs for damage intersecting path 2–6 display a closely clustered pattern.  
COP: coefficients of projection.

The time-dependent parameters for path 2–6 are shown in Figures 9(a)–(c). Wavelet, Chebyshev, and trigonometric orthogonal basis functions are used, respectively. Figure 9(a) shows the four time-varying model parameters  $\alpha_1$ ,  $\alpha_2$ ,  $\alpha_3$ , and  $\alpha_4$  for different structural states ( $a_i[t]$  from equation (1)), namely: healthy and damage level 1 through damage level 4 for wavelet basis functions. For each parameter (such as  $\alpha_1$ ) and each structural state (such as damage level 1), 20 realizations are shown. All the realizations of a specific structural state form a band along the entire time span, and different structural states can be visualized by examining the time-varying model parameters. However, from Figure 9(b), for the Chebyshev basis functions and time-varying parameters  $\alpha_1$  and  $\alpha_4$ , realizations of different structural states overlap with each other over the entire time span. From Figure 9(c), for trigonometric basis functions, for time-varying parameter  $\alpha_4$ , the realizations of different structural states are seen to be well separated, although they overlap with each other at certain time instants.

Figure 10(a)–(c) shows the time-varying model parameters ( $a_i[t]$  from equation (1)) with their respective  $\pm 2$  standard deviation confidence intervals for wavelet, Chebyshev and trigonometric basis functions, respectively, for damage intersecting path 2–6. The experimental confidence bounds were obtained from the 20 experimental signals (realizations) of the healthy state.

The time-varying mean parameters are shown as solid blue lines, and the  $\pm 2$  standard deviation confidence intervals are shown as shaded regions for the parameters  $\alpha_1$ ,  $\alpha_2$ ,  $\alpha_3$ , and  $\alpha_4$ . The black solid lines represent estimated parameters from the healthy state. The solid red lines represent estimated time-varying

parameters from damage level 1. Note that the time-varying parameters from the healthy state (black solid line) remain within the  $\pm 2$  standard deviation confidence interval at each time instant. However, the time-varying parameters from damage level 1 (solid red lines) go outside the  $\pm 2$  standard deviation confidence interval at certain time instants for the four parameters.

### Results from COP-based damage diagnosis

Figure 11 illustrates the characteristic quantity evaluation for path 1–4 using wavelet, Chebyshev, and trigonometric orthogonal basis functions. The sample covariance matrix for all cases was derived from 20 trial signals of the healthy state, and all COPs were utilized. Precise damage detection was achieved across the three orthogonal basis functions used. The  $\alpha$  level was set at  $1 \times 10^{-3}$  for the wavelet basis function and  $1 \times 10^{-12}$  for both the Chebyshev and trigonometric basis functions.

Figure 12 demonstrates the diagnosis results for path 2–6 based on wavelet, Chebyshev, and trigonometric basis functions. Accurate damage detection performance can be observed for the three basis functions considered. The  $\alpha$  level for each basis function was set at  $1 \times 10^{-12}$ .  $\alpha$  levels for different path and basis functions can be found in Table 2.

Results for damage identification for various structural states considered in this study are shown in Figure 13. Only the results for path 1–4 are shown. Wavelet basis functions and the experimental sample covariance matrix were used. The proposed FS-TAR-based method achieved accurate damage identification with no damage misclassifications. For instance, when identifying damage level 2, the characteristic quantities

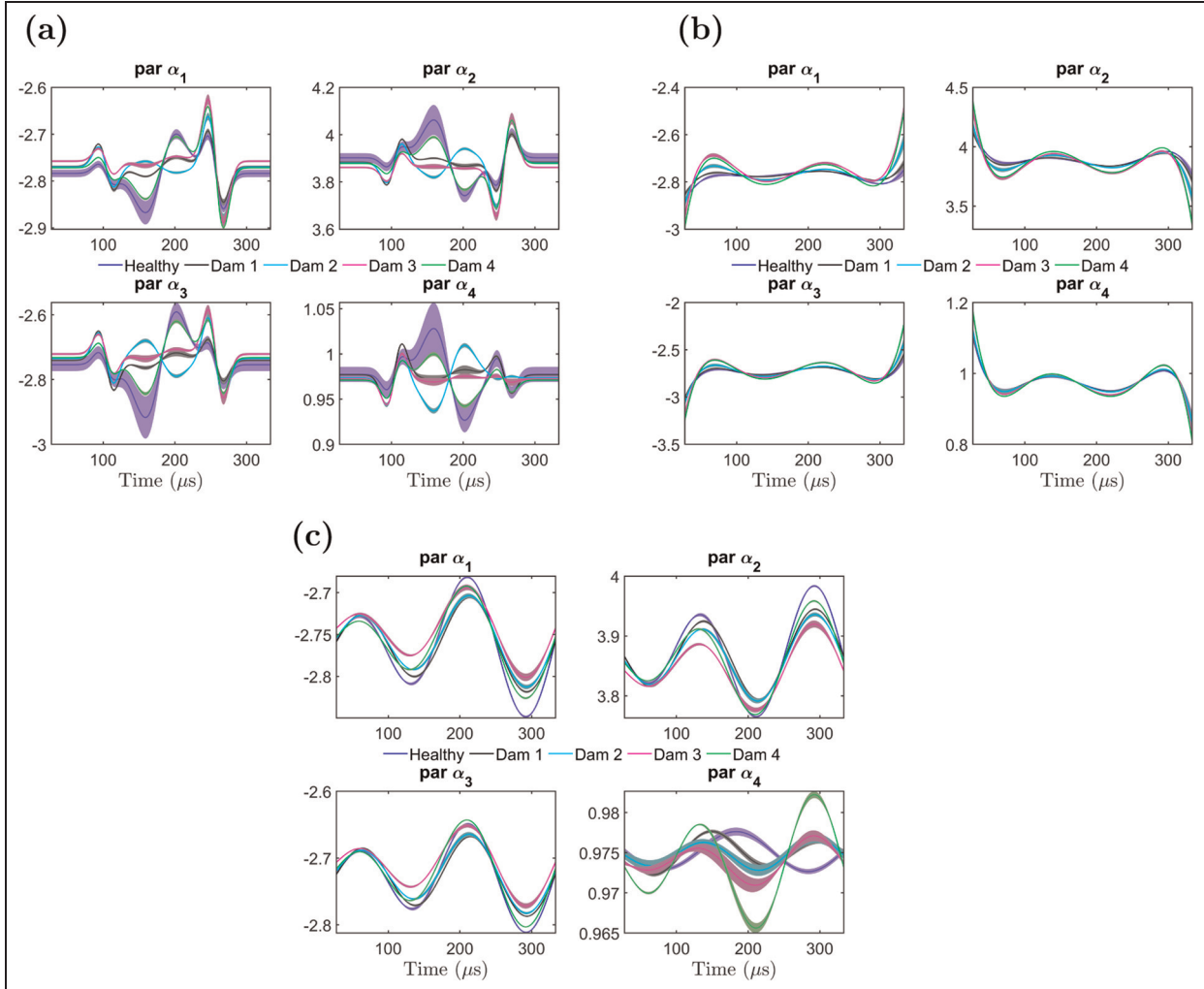


**Figure 9.** The mean and the corresponding  $\pm 2$  standard deviation confidence intervals of the time-dependent model parameters ( $a_i[t]$  from equation (1)) of the FS-TAR model for various structural states of the aluminum coupon for damage intersecting path 2–6, are illustrated for different basis functions: (a) wavelet, (b) Chebyshev, and (c) trigonometric. The time-dependent confidence intervals of the model parameters form a distinct band, and this distinction is more pronounced for the case of wavelet orthogonal basis functions (a).

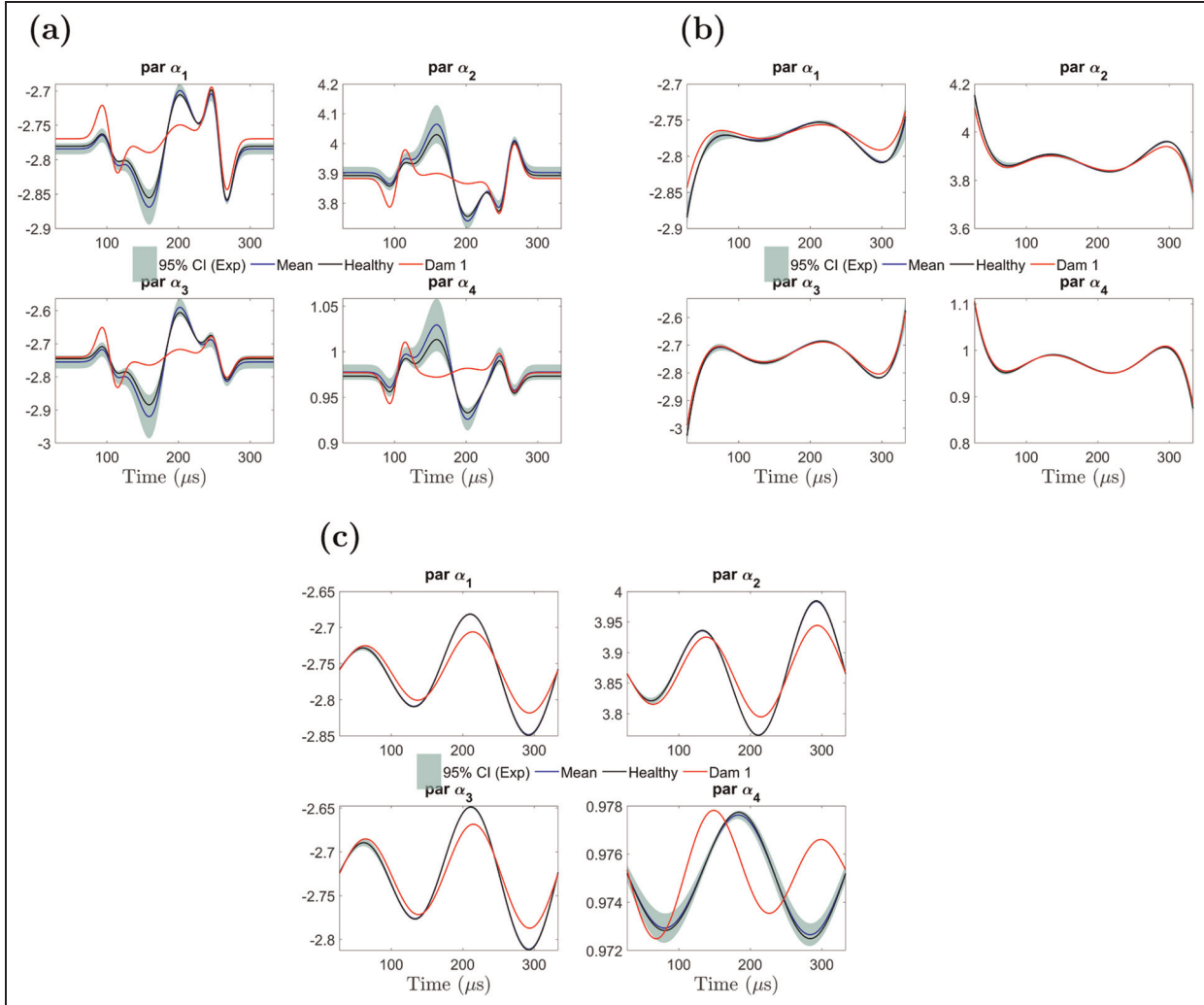
of the specified damage level 2 lie within the statistical threshold.

Table 3 succinctly presents the damage diagnosis results using wavelet, Chebyshev, and trigonometric basis functions for the two indicative path (path 2–6 and path 1–4) and the associated covariance matrices. 0/20 means that damage detection is being performed, and there is zero instance of false alarms (for healthy case) or missed damage (for damage level 1, 2, 3, or 4) out of 20 instances. (0, –, 0, 0) means that damage identification is being performed, and damage level 2 is being identified. There are zero instances of damage misclassifications for damage level 1, 3 and 4. (–, 20, 20, 0) would mean that damage level 1 is being identified and 20 instances of damage level 2 and 20 instances of damage level 3 are being misclassified, that

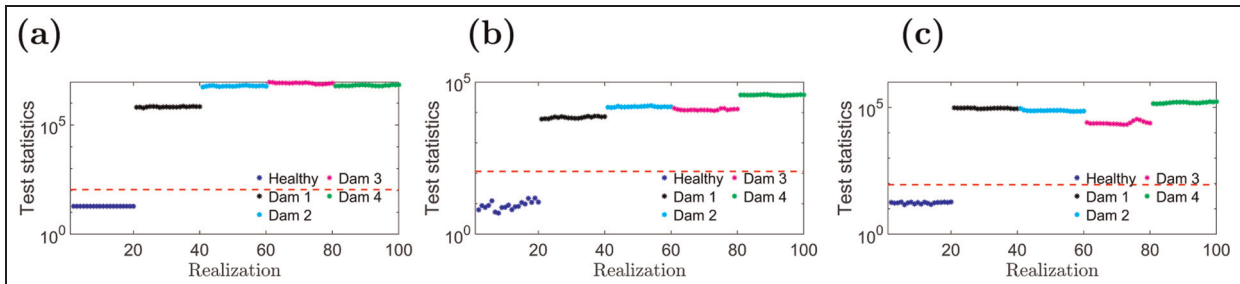
is, their test statistics do not exceed the confidence bound. Ideally, we want the test statistics for the identified damage level to remain within the confidence bound, while the test statistics for all other cases (states) fall outside the confidence bound. Accurate damage detection was achieved for all three basis functions. However, during damage identification, there are instances of damage misclassifications for wavelet and Chebyshev basis functions. With trigonometric basis functions, accurate damage diagnosis (detection and identification) was achieved.

#### Results from time-varying parameter-based damage diagnosis

Figure 14 and 15(a)–(c) displays time-varying damage detection using wavelet, Chebyshev, and trigonometric



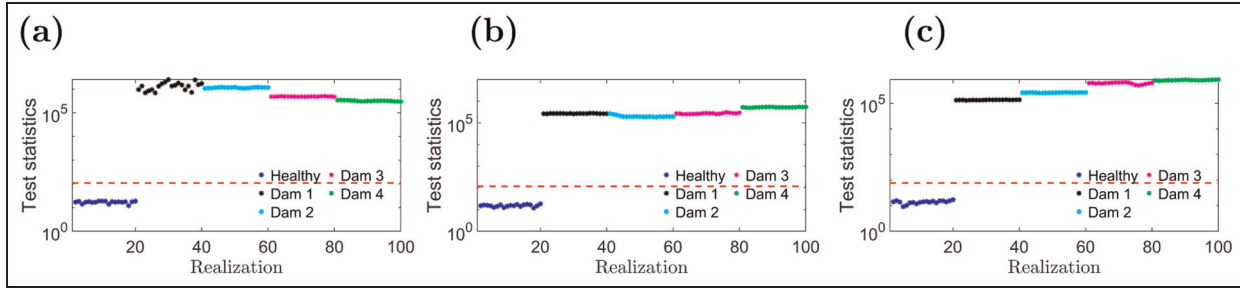
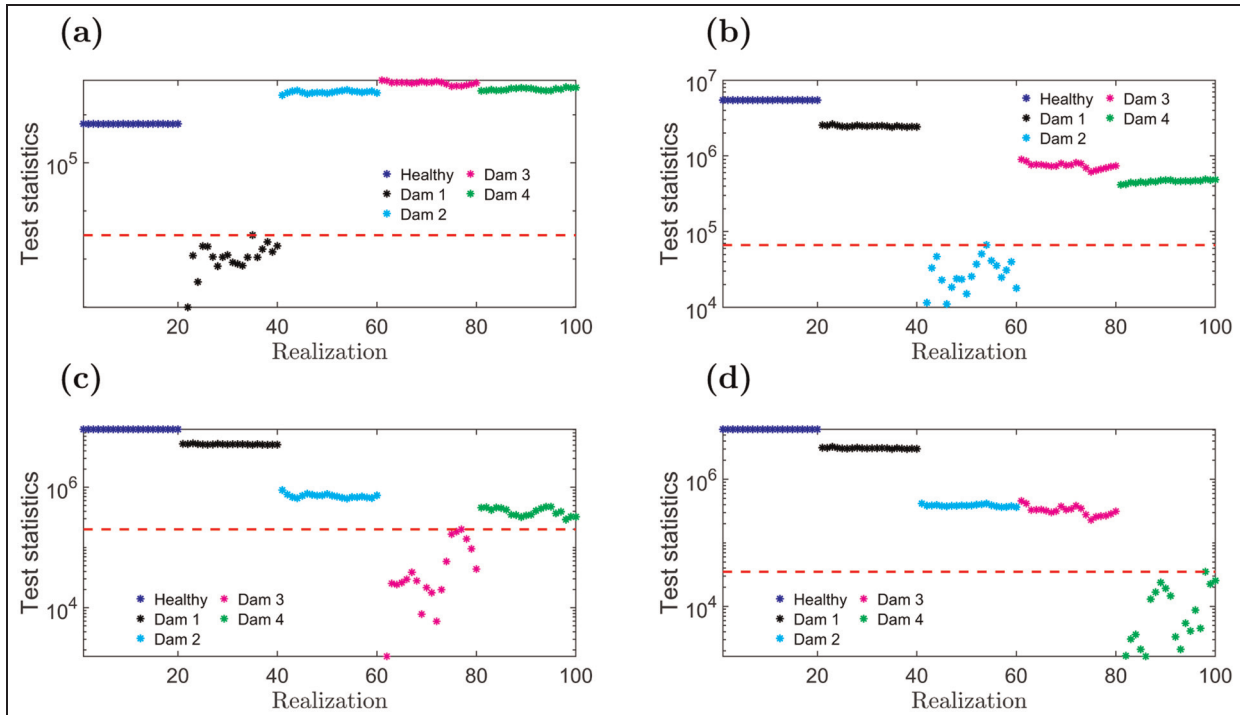
**Figure 10.** The time-dependent model parameters ( $a_i[t]$  from equation (1)) in nominal state, associated confidence bound, and the parameter evolution of a damaged state are presented for the damage intersecting path 2–6: (a) wavelet (b) Chebyshev; (c) trigonometric orthogonal basis functions. The parameters are represented by dark solid lines, with the corresponding  $\pm 2$  standard deviations shown as light shaded regions. The parameters for the healthy case remain within the CI while the parameter of the damage level I goes outside the CI.



**Figure 11.** The detection methods based on (a) wavelet, (b) Chebyshev, and (c) trigonometric orthogonal basis functions are shown (path 1–4). The sample covariance from the nominal state is employed. The three basis functions achieve accurate damage detection, as evidenced by the test statistics of the healthy trials (blue dots) remaining below the threshold (red lines).

**Table 2.**  $\alpha$ -levels used for COP-based damage detection for various basis functions and wave propagation path.

Functional bases	Path	Covariance	$\alpha$ -level
Wavelet basis	1–4	Experimental	$1 \times 10^{-3}$
	2–6		$1 \times 10^{-12}$
Chebyshev basis	1–4	Experimental	$1 \times 10^{-12}$
	2–6		$1 \times 10^{-12}$
Trigonometric basis	1–4	Experimental	$1 \times 10^{-12}$
	2–6		$1 \times 10^{-12}$

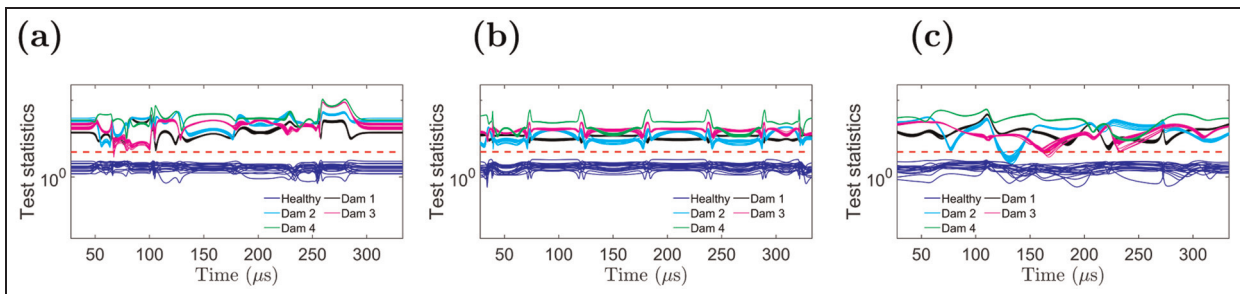
**Figure 12.** The detection methods based on (a) wavelet, (b) Chebyshev, and (c) trigonometric orthogonal basis functions are presented (path 2–6). This assessment utilizes the sample covariance matrix from the structure's nominal state.**Figure 13.** The damage identification results for path 1–4 are shown: (a) damage level 1, (b) damage level 2, (c) damage level 3, and (d) damage level 4. The wavelet orthogonal basis functions and the sample covariance matrix are used.

**Table 3.** COP-based damage diagnosis results for various orthogonal basis functions, guided wave propagation paths, and covariance used.

Functional bases	Path	Covariance	Damage detection				
			False alarms		Missed damage		
			Healthy	Dam 1	Dam 2	Dam 3	Dam 4
Wavelet basis	1–4	Experimental	0/20	0/20	0/20	0/20	0/20
	1–4	Theoretical	0/20	0/20	0/20	0/20	0/20
	2–6	Experimental	0/20	0/20	0/20	0/20	0/20
	2–6	Theoretical	0/20	0/20	0/20	0/20	0/20
Chebyshev basis	1–4	Experimental	0/20	0/20	0/20	0/20	0/20
	1–4	Theoretical	0/20	0/20	0/20	0/20	0/20
	2–6	Experimental	0/20	0/20	0/20	0/20	0/20
	2–6	Theoretical	0/20	0/20	0/20	0/20	0/20
Trigonometric basis	1–4	Experimental	0/20	0/20	0/20	0/20	0/20
	1–4	Theoretical	0/20	0/20	0/20	0/20	0/20
	2–6	Experimental	0/20	0/20	0/20	0/20	0/20
	2–6	Theoretical	0/20	0/20	0/20	0/20	0/20

Functional bases	Path	Covariance	Damage identification			
			Damage misclassifications			
			Dam 1	Dam 2	Dam 3	Dam 4
Wavelet basis	1–4	Experimental	(−0,0,0)	(0,−0,0)	(0,0,−0)	(0,0,0,−)
	1–4	Theoretical	(−0,0,0)	(0,−0,0)	(0,0,−0)	(0,0,0,−)
	2–6	Experimental	(−20,20,0)	(0,−0,0)	(0,0,−0)	(0,0,0,−)
	2–6	Theoretical	(−0,0,0)	(0,−0,0)	(0,0,−0)	(0,0,0,−)
Chebyshev basis	1–4	Experimental	(−0,0,0)	(0,−0,0)	(0,0,−0)	(0,0,0,−)
	1–4	Theoretical	(−0,0,0)	(0,−6,0)	(0,18,−0)	(0,0,0,−)
	2–6	Experimental	(−0,0,0)	(0,−0,0)	(0,0,−0)	(0,0,0,−)
	2–6	Theoretical	(−0,0,0)	(0,−0,0)	(0,0,−0)	(0,0,0,−)
Trigonometric basis	1–4	Experimental	(−0,0,0)	(0,−0,0)	(0,0,−0)	(0,0,0,−)
	1–4	Theoretical	(−0,0,0)	(0,−0,0)	(0,0,−0)	(0,0,0,−)
	2–6	Experimental	(−0,0,0)	(0,−0,0)	(0,0,−0)	(0,0,0,−)
	2–6	Theoretical	(−0,0,0)	(0,−0,0)	(0,0,−0)	(0,0,0,−)



**Figure 14.** The damage detection and the evolution of the time-dependent characteristic quantity based on (a) wavelet; (b) Chebyshev; and (c) trigonometric orthogonal basis functions are shown for path 1–4.

basis functions, respectively, for path 1–4 and path 2–6. Twenty trial signals from the structure's nominal state were utilized to obtain the sample covariance. The four time-dependent parameters  $\alpha_1$ ,  $\alpha_2$ ,  $\alpha_3$ , and  $\alpha_4$  were used with the corresponding time-varying sample

covariance. For all time instants, the time-dependent characteristic quantities for the healthy state remained within the statistical threshold while for different damaged states, the quantities crossed the statistical threshold. Consequently, accurate damage detection

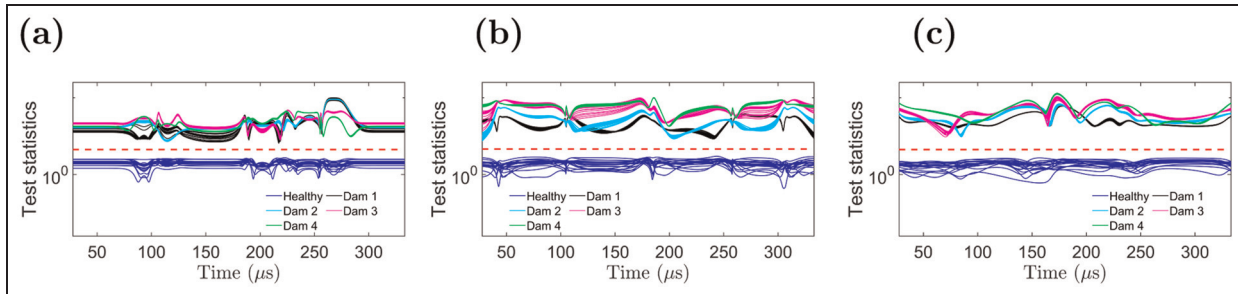


**Figure 15.** The damage detection and the evolution of the time-dependent characteristic quantity based on (a) wavelet; (b) Chebyshev; and (c) trigonometric orthogonal basis functions are shown for path 2–6. The sample covariance was used.

**Table 4.**  $\alpha$ -levels used for damage detection with time-dependent model parameters.

Functional bases	Path	Covariance	$\alpha$ -level
Wavelet basis	1–4	Experimental	$1 \times 10^{-4}$
	2–6		$1 \times 10^{-4}$
Chebyshev basis	1–4	Experimental	$1 \times 10^{-4}$
	2–6		$1 \times 10^{-4}$
Trigonometric basis	1–4	Experimental	$1 \times 10^{-4}$
	2–6		$1 \times 10^{-4}$

performance could be obtained using the sample covariance. Table 4 summarizes the  $\alpha$ -levels used for damage detection using time-dependent parameters.

Damage identification results for path 1–4 are presented in Figure 16. This particular representative case uses the time-dependent parameters from the Chebyshev basis functions. Twenty trial signals, as before, were utilized to obtain the time-dependent sample covariance. Accurate damage identification was accomplished with no damage misclassification. Table 5 presents the damage diagnosis results with the time-dependent parameters using the three orthogonal basis functions. (0,–,0,0) means damage level 2 is being identified and there is zero damage misclassification for damage level 1, 3, and 4. Additionally, (0,20,–,13) would mean damage level 3 is being identified, and there are 20 realizations of damage level 2 and 13 realizations of damage level 4 that do not go outside the threshold for a single time instance, and as such have damage misclassification. Only Chebyshev basis functions have missed damage and damage misclassification when using FS-TAR model-based covariance for damage diagnosis using time-dependent model parameters. Wavelet and trigonometric basis functions show excellent results for damage diagnosis using time-dependent parameters with no missed damage and damage misclassification for the three situations considered. From Tables 3 and 5, it is observed that by utilizing time-varying parameter-based approach, damage misclassifications for COP-based approach with wavelet basis functions can be improved.

## Discussion

In this work, FS-TAR model was used to model the high-frequency dynamics or vibration of the plate, and then the identified model was employed to perform damage diagnosis in the aluminum structure. Guided wave or Lamb wave propagation is the result of the high-frequency vibration of the plate-like structures.<sup>52</sup> In the present work, this high-frequency vibration of the aluminum coupon (or ultrasonic wave propagation) was induced by exciting a permanently installed PZT disk transducer by applying a narrow-band 5-peak tone burst actuation signal. The propagated disturbance or vibration is captured by another PZT disk transducer. If there is a crack or damage present within the structure, the amplitude and phase of the  $S_0$  or  $A_0$  mode or the first arrival wave packet are changed due to the interaction with the damage. In the traditional approach, only this initial portion of the signal is used for damage diagnosis, and the rest of the signal is discarded.

The dispersion curve for the specific 6061 aluminum plate used in this study was obtained by using the MATLAB-based software "wavescope"<sup>5</sup> and is shown in Figure 3(b). From the dispersion curve, for the actuation frequency 250 KHz and plate thickness 2.36 mm, the calculated wave speed (phase velocity) for the first symmetric mode is 5328 m/s. From Figure 2(b), the distance between the sensor 1 and 4 is 5 inches (0.127 m; path 1–4) and the distance between the sensor 2 and 6 is 5.22 inches (0.132 m). Thus, the

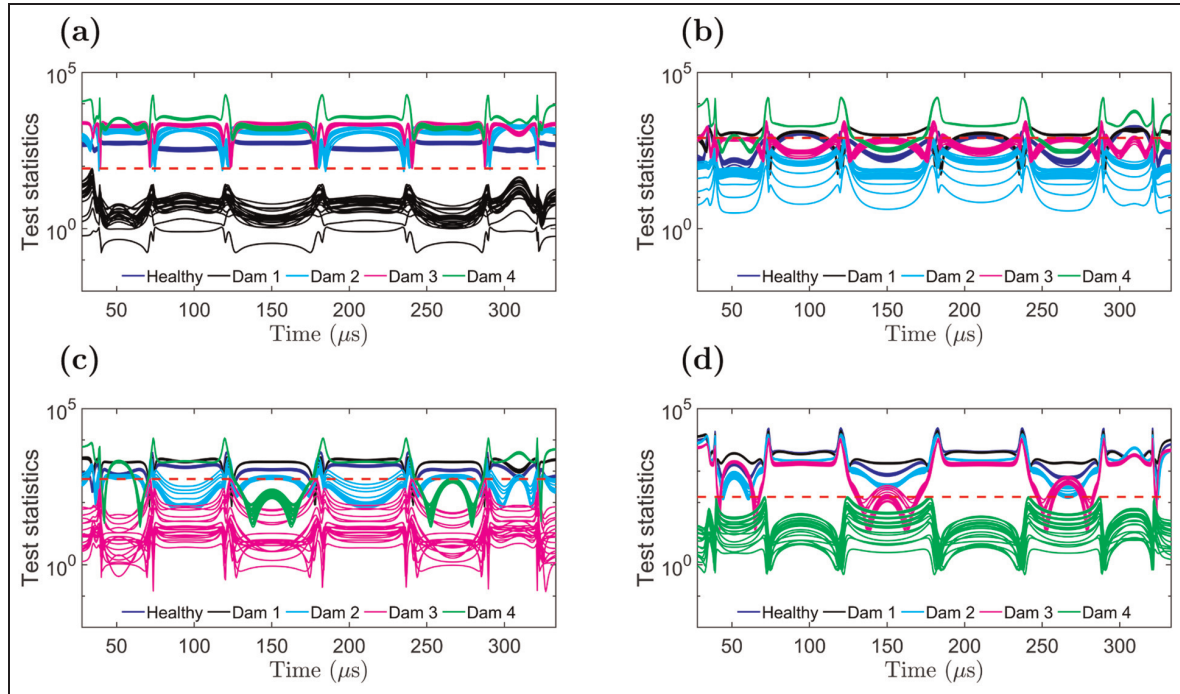


**Figure 16.** Damage identification for path 1–4 is shown by utilizing the time-dependent model parameters. Chebyshev basis functions and sample time-dependent covariance were used. Cases for damage level 1 through 4 are shown.

**Table 5.** Damage diagnosis results for the aluminum coupon using the time-varying model parameters.

Functional bases	Path	Covariance	Damage detection				
			False alarms		Missed damage		
			Healthy		Damage 1	Damage 2	Damage 3
Wavelet basis	1–4	Experimental	0/20	0/20	0/20	0/20	0/20
	1–4	Theoretical	0/20	0/20	0/20	0/20	0/20
	2–6	Experimental	0/20	0/20	0/20	0/20	0/20
	2–6	Theoretical	0/20	0/20	0/20	0/20	0/20
Chebyshev basis	1–4	Experimental	0/20	0/20	0/20	0/20	0/20
	1–4	Theoretical	0/20	0/20	0/20	0/20	0/20
	2–6	Experimental	0/20	0/20	0/20	0/20	0/20
	2–6	Theoretical	0/20	9/20	0/20	0/20	0/20
Trigonometric basis	1–4	Experimental	0/20	0/20	0/20	0/20	0/20
	1–4	Theoretical	0/20	0/20	0/20	0/20	0/20
	2–6	Experimental	0/20	0/20	0/20	0/20	0/20
	2–6	Theoretical	0/20	0/20	0/20	0/20	0/20
Functional bases		Path	Covariance	Damage identification			
				Damage misclassifications			
				Damage 1	Damage 2	Damage 3	Damage 4
Wavelet basis	1–4	Experimental	(−,0,0,0)	(0,−,0,0)	(0,0,−,0)	(0,0,0,−)	
	1–4	Theoretical	(−,0,0,0)	(0,−,0,0)	(0,0,−,0)	(0,0,0,−)	
	2–6	Experimental	(−,0,0,0)	(0,−,0,0)	(0,0,−,0)	(0,0,0,−)	
	2–6	Theoretical	(−,0,0,0)	(0,−,0,0)	(0,0,−,0)	(0,0,0,−)	
Chebyshev basis	1–4	Experimental	(−,0,0,0)	(0,−,0,0)	(0,0,−,0)	(0,0,0,−)	
	1–4	Theoretical	(−,0,0,0)	(0,−,0,14)	(0,20,−,13)	(0,0,0,−)	
	2–6	Experimental	(−,0,0,0)	(0,−,0,0)	(0,0,−,0)	(0,0,0,−)	
	2–6	Theoretical	(−,0,0,0)	(20,−,0,0)	(0,0,−,0)	(0,0,0,−)	
Trigonometric basis	1–4	Experimental	(−,0,0,0)	(0,−,0,0)	(0,0,−,0)	(0,0,0,−)	
	1–4	Theoretical	(−,0,0,0)	(0,−,0,0)	(0,0,−,0)	(0,0,0,−)	
	2–6	Experimental	(−,0,0,0)	(0,−,0,0)	(0,0,−,0)	(0,0,0,−)	
	2–6	Theoretical	(−,0,0,0)	(0,−,0,0)	(0,0,−,0)	(0,0,0,−)	

travel time for the  $S_0$  mode from sensor 1 to 4 is 23.83  $\mu\text{s}$ . On the other hand, the travel time required for the wave from sensor 2 to 6 is 24.77  $\mu\text{s}$  ( $S_0$  mode). Additionally, the distance from sensor 1 to the left edge is 1.5 inches (0.038 m) and the guided wave (first symmetric mode) takes 7.13  $\mu\text{s}$  to reach the left edge. Again, from the dispersion curve, for the actuation frequency 250 kHz and plate thickness 2.36 mm, the calculated wave speed (phase velocity) for the  $A_0$  mode is 1977 m/s. With this speed, the first anti-symmetric mode takes 64  $\mu\text{s}$  to travel from sensor 1 to 4 and 69  $\mu\text{s}$  from sensor 2 to 6. With this analysis, it is evident that (for path 1–4) by the time the first anti-symmetric mode reaches sensor 4 from sensor 1, the reflections from the boundary of the plate also reach sensor 4. As a result, with this geometrical configuration of the aluminum plate, the starting and ending point of the first anti-symmetric mode is difficult to isolate. In Figure 2(c), top and middle subplot, note that until 50  $\mu\text{s}$ , signals from different structural states have no visible change due to the added weights. However, noticeable distinctions in the received signals can be observed from 230 to 332  $\mu\text{s}$ . This part of the signals is the back-and-forth reflections from the boundary and may be thought of as standing waves in the plate. A nice separation between the  $S_0$  and  $A_0$  mode could be obtained when the plate is large, sensors are placed at least 5 inches apart and the reflections from the boundary do not interfere with the  $S_0$  and  $A_0$  mode. However, these states are difficult to meet in practical applications.

To circumvent this difficulty, the focus has been placed on analyzing the underlying dynamics of the complete signals, rather than isolating the  $S_0$  and  $A_0$  wave packets and finding change in these wave packets due to damage. The parameters  $a_i[t]$  or the COP  $\theta$  of the FS-TAR model essentially encapsulate the structural dynamics due to the guided wave propagation. Any change in the dynamics of the structure due to the added mass (present work) or the presence of damage within the structure would be manifested in the model parameters. This fact has been demonstrated in Figures 5 and 6.

Although it is difficult to visually recognize the amplitude or phase differences in the guided wave signals due to the effect of damage, such as in Figure 2(c), a clear distinguishable pattern can be observed in Figures 7 and 9, where the COPs and the time-dependent parameters are shown, respectively. Among the three families of basis functions investigated, the wavelet basis functions result in better separation of model parameters and thus better performance for damage detection and identification. A distinguishable characteristic of the COP is that its theoretical probability distribution is known from the estimator's

asymptotic properties. Thus, the theoretical confidence bound of the time-varying parameters can be obtained from the theoretical probability distributions of the COP vector and can be invoked to render interpretable results.

The estimated COPs and the time-dependent parameters are subsequently utilized to obtain the “test statistics” or the characteristic quantity  $Q$  (equation (22)), which forms the basis of the damage diagnosis algorithm. The theoretical probability distribution of this quantity  $Q$  is the Chi-squared distribution, from which a damage detection threshold based on the type I error probability can be provided. The estimated quantity  $Q$  is a function of the covariance matrix  $P_\theta$  or  $P[t]$ . As explained in section “COP estimation,” both the theoretical and experimental covariance matrix can be used. The theoretical covariance matrix for the coefficient of projection was obtained from equation (20). The theoretical covariance matrix for the time-dependent parameters can be obtained by sampling from the multivariate Gaussian distribution according to equation (21). The experimental covariance was obtained from different trials or realizations (20 signals) of the experimental guided wave signals. The obtained theoretical confidence bound may overestimate the experimental variability. As a result, only the damage diagnosis results using the experimental sample covariance matrix are presented. Additionally, Tables 3 and 5 present the damage diagnosis results for all possible cases in a compact way.

The wavelet basis functions provided the best results and are recommended for future use for ultrasonic guided wave-based damage diagnosis. The Gaussian wavelets were used in the present study and may be better suited for modeling the ultrasonic signals excited by a 5-peak tone burst actuation. As long as there is a change in dynamics due to the existence of a crack or damage, the method would be able to detect it. One caveat of this method is that the threshold based on the type I error probability might be too low such as  $\alpha = 1e - 12$ . However, for wavelet basis functions, the  $\alpha$ -level is on the order of  $1e - 3$ , which is a standard value. It is to be mentioned here that, the  $\alpha$ -level only affects the interpretation of the results for damage diagnosis. The model parameters and the test statistics would be different for healthy and damaged cases with a margin as long as there is an observable change in dynamics and as long as that dynamics is not masked by the environmental effects.

As guidelines for future research, it can be investigated how the model parameters and diagnostic capability of the method vary with the presence of varying environmental and operational states compared to the pristine case. The effect of temperature and load variation can be investigated and the associated uncertainty

can be quantified. In the present paper, a reversible damage configuration is presented. In future works, irreversible damage, progression of fatigue cracks in metallic structures, and matrix cracking leading to delamination in composite structures will be considered.

Care should be taken in choosing the estimator for estimating the model parameters or the COP vector. In this work, maximum-likelihood estimator was employed due to its consistency and asymptotic efficiency. The derivation of the estimator asymptotic properties can be found in Kopsaftopoulos.<sup>70</sup>

## Conclusion

The present work developed and experimentally evaluated an FS-TAR model-based statistical damage diagnosis framework for ultrasonic guided wave-based damage detection and identification. FS-TAR models employ deterministic parameter evolution methods, wherein time-varying model parameters and variances are projected onto orthogonal basis functions. Three families of basis functions—wavelet, Chebyshev, and trigonometric—were explored, and their damage diagnosis performance was evaluated. Detailed methodologies for estimating projection coefficients, model identification, and validation were provided. Model identification was executed using a GA-based optimization approach, noted for its rapid convergence yet potential susceptibility to local minima. A heuristic method was also introduced as an alternative, emphasizing the necessity of expert intervention. Two damage diagnosis schemes—based on time-invariant projection coefficients and time-varying parameters—were presented and comparatively assessed using the same dataset. Results indicate that employing the time-varying parameter approach significantly reduces misclassification errors associated with the wavelet-based projection coefficients, whereas this improvement is limited when using Chebyshev basis functions. The robustness of both approaches was tested with experimental and model-based covariance matrices across representative damage scenarios, including damage intersecting and non-intersecting paths. Computational efficiency was demonstrated by the short computational time (13.46 s) needed to estimate projection coefficients for 601 sample-long signals using standard hardware specifications (Intel Core-i7, 2.1 GHz, 16 GB RAM). Apart from initial model identification, the FS-TAR method requires no additional training, making it highly suitable for online damage diagnosis applications.

FS-TAR modeling explicitly considers the non-stationary characteristics of guided waves, utilizing both the initial wave packets and reflected (coda)

waves. The inherent model uncertainty, quantified using the asymptotic joint probability distributions of parameter estimates, facilitates the formulation of a probabilistic framework for damage diagnosis. This approach represents a significant advancement over traditional deterministic methods, offering enhanced reliability and interpretability for guided wave-based damage detection and identification. The use of the complete wave signal, that is, including the reflections, is also an important characteristic of the developed modeling and diagnostic framework.

Future research directions could include examining how environmental and operational states impact model parameters relative to pristine states, along with their effects on damage diagnosis accuracy and robustness. Investigating uncertainties due to temperature and load variations, as well as extending analyses to irreversible damage scenarios—such as fatigue crack progression, corrosion, or impact-induced damage—would further strengthen the method's applicability.

## Declaration of conflicting interests

The authors declared no potential conflicts of interest with respect to the research, authorship, and/or publication of this article.

## Funding

The authors disclosed receipt of the following financial support for the research, authorship, and/or publication of this article: This work is supported by the U.S. Air Force Office of Scientific Research (AFOSR) grant number: FA9550-19-1-0054.

## ORCID iDs

Shabbir Ahmed  <https://orcid.org/0000-0001-8296-6025>  
Fotis Kopsaftopoulos  <https://orcid.org/0000-0001-8795-3725>

## References

1. Farrar CR and Worden K. An introduction to structural health monitoring. *Royal Soc Philos Trans Math Phys Eng Sci* 2007; 365: 303–315.
2. Ihn J and Chang F-K. Detection and monitoring of hidden fatigue crack growth using a built-in piezoelectric sensor/actuator network, Part I: Diagnostics. *Smart Mater Struct* 2004; 13: 609–620.
3. Ihn J and Chang F-K. Detection and monitoring of hidden fatigue crack growth using a built-in piezoelectric sensor/actuator network, Part II: Validation through riveted joints and repair patches. *Smart Mater Struct* 2004; 13: 621–630.
4. Li L, Mei H, Haider MF, et al. Guided wave field calculation in anisotropic layered structures using normal mode expansion method. *Smart Struct Syst* 2020; 26(2): 157–174.

5. Giurgiutiu V. *Structural health monitoring: With piezoelectric wafer active sensors*. Amsterdam, The Netherlands: Elsevier, 2007.
6. Mei H, Haider MF, Joseph R, et al. Recent advances in piezoelectric wafer active sensors for structural health monitoring applications. *Sensors* 2019; 19(2): 383.
7. Ahmed S and Kopsaftopoulos F. Active sensing ultrasonic guided wave-based damage diagnosis via stochastic stationary time-series models. *Struct Health Monit* 2023; 23(4): 2559–2595.
8. Amer A and Kopsaftopoulos FP. Statistical guided-waves-based structural health monitoring via stochastic non-parametric time series models. *Struct Health Monit* 2021; 21(3): 1139–1166.
9. Amer A and Kopsaftopoulos F. Gaussian process regression for active sensing probabilistic structural health monitoring: experimental assessment across multiple damage and loading scenarios. *Struct Health Monit* 2023; 22(2): 1105–1139.
10. Roy S, Lonkar K, Janapati V, et al. A novel physics-based temperature compensation model for structural health monitoring using ultrasonic guided waves. *Struct Health Monit* 2014; 13(3): 321–342.
11. Janapati V, Kopsaftopoulos F, Li F, et al. Damage detection sensitivity characterization of acousto-ultrasound-based structural health monitoring techniques. *Struct Health Monit* 2016; 15(2): 143–161.
12. Song G, Gu H and Mo Y-L. Smart aggregates: multi-functional sensors for concrete structures—a tutorial and a review. *Smart Mater Struct* 2008; 17(3): 033001.
13. Wang F, Huo L and Song G. A piezoelectric active sensing method for quantitative monitoring of bolt loosening using energy dissipation caused by tangential damping based on the fractal contact theory. *Smart Mater Struct* 2017; 27(1): 015023.
14. Tibaduiza DA, Mujica LE, Rodellar J, et al. Structural damage detection using principal component analysis and damage indices. *J Intell Mater Syst Struct* 2016; 27(2): 233–248.
15. Lize E, Rébillat M, Mechbal N, et al. Optimal dual-PZT sizing and network design for baseline-free SHM of complex anisotropic composite structures. *Smart Mater Struct* 2018; 27(11): 115018.
16. Qiu J, Li F, Abbas S, et al. A baseline-free damage detection approach based on distance compensation of guided waves. *J Low Freq Noise Vib Act Control* 2019; 38(3–4): 1132–1148.
17. Liu S, Zhu J and Wu Z. Implementation of coda wave interferometry using Taylor series expansion. *J Nondestruct Eval* 2015; 34: 1–6.
18. Fröjd P and Ulriksen P. Frequency selection for coda wave interferometry in concrete structures. *Ultrasonics* 2017; 80: 1–8.
19. Snieder R, Grêt A, Douma H, et al. Coda wave interferometry for estimating nonlinear behavior in seismic velocity. *Science* 2002; 295(5563): 2253–2255.
20. Lim HJ, Lee H, Skinner T, et al. Fatigue damage detection and growth monitoring for composite structure using coda wave interferometry. *Struct Control Health Monit* 2021; 28(3): e2689.
21. Jin H, Yan J, Li W, et al. Monitoring of fatigue crack propagation by damage index of ultrasonic guided waves calculated by various acoustic features. *Appl Sci* 2019; 9(20): 4254.
22. Xu B, Zhang T, Song G, et al. Active interface debonding detection of a concrete-filled steel tube with piezoelectric technologies using wavelet packet analysis. *Mech Syst Signal Proc* 2013; 36(1): 7–17.
23. Hua J, Cao X, Yi Y, et al. Time-frequency damage index of Broadband Lamb wave for corrosion inspection. *J Sound Vibr* 2020; 464: 114985.
24. Su Z, Zhou C, Hong M, et al. Acousto-ultrasonics-based fatigue damage characterization: linear versus nonlinear signal features. *Mech Syst Signal Proc* 2014; 45(1): 225–239.
25. Ibáñez F, Baltazar A and Mijarez R. Detection of damage in multiwire cables based on wavelet entropy evolution. *Smart Mater Struct* 2015; 24(8): 085036.
26. Rojas E, Baltazar A and Loh K. Damage detection using the signal entropy of an ultrasonic sensor network. *Smart Mater Struct* 2015; 24(7): 075008.
27. Qiu L, Fang F, Yuan S, et al. An enhanced dynamic Gaussian mixture model-based damage monitoring method of aircraft structures under environmental and operational conditions. *Struct Health Monit* 2019; 18(2): 524–545.
28. Haynes C, Todd MD, Flynn E, et al. Statistically-based damage detection in geometrically-complex structures using ultrasonic interrogation. *Struct Health Monit* 2013; 12(2): 141–152.
29. Liao W, Sun H, Wang Y, et al. A novel damage index integrating piezoelectric impedance and ultrasonic guided wave for damage monitoring of bolted joints. *Struct Health Monit* 2023; 22(5): 3514–3533.
30. Si L and Li Z. Online structural state assessment for aerospace composite structures using an acousto-ultrasonics-based multi-damage index identification approach. *Struct Health Monit* 2020; 19(6): 1790–1807.
31. An Y-K and Sohn H. Integrated impedance and guided wave based damage detection. *Mech Syst Signal Proc* 2012; 28: 50–62.
32. De Luca A, Caputo F, Khodaei ZS, et al. Damage characterization of composite plates under low velocity impact using ultrasonic guided waves. *Compos B Eng* 2018; 138: 168–180.
33. Wang K, Zhang J, Shen Y, et al. Defect detection in guided wave signals using nonlinear autoregressive exogenous method. *Struct Health Monit* 2022; 21(3): 1012–1030.
34. Tu XL, Pyle RJ, Croxford AJ, et al. Potential and limitations of NARX for defect detection in guided wave signals. *Struct Health Monit* 2022; 22(3): 1863–1875.

35. Da Silva S, Villani LG, Rébillat M, et al. Gaussian process NARX model for damage detection in composite aircraft structures. *J Nondestruct Eval Diagn Progn Eng Syst* 2022; 5(1): 011007.
36. Ahmed S and Kopsaftopoulos F. Active sensing acousto-ultrasound SHM via stochastic non-stationary time series models. In: *European workshop on structural health monitoring*. Cham: Springer, 2023, pp. 256–266.
37. Ahmed S and Kopsaftopoulos F. Statistical active-sensing structural health monitoring via stochastic time-varying time series models. In: *2022 American Control Conference (ACC)*. New York, NY: IEEE, 2022, pp. 3599–3606.
38. Ahmed S and Kopsaftopoulos F. Stochastic identification of guided wave propagation under ambient temperature via non-stationary time series models. *Sensors* 2021; 21(16): 5672.
39. Ahmed S and Kopsaftopoulos F. Time-varying identification of guided wave propagation under varying temperature via non-stationary time series models. arXiv preprint arXiv:2201.04721, 2022.
40. Kopsaftopoulos FP and Fassois SD. Experimental assessment of time series methods for structural health monitoring (SHM). In: *Proceedings of the 4th European workshop on structural health monitoring (EWSHM)*, Cracow, Poland, 2008.
41. Kopsaftopoulos FP and Fassois SD. Vibration-based structural damage detection and precise assessment via stochastic functionally pooled models. *Key Eng Mater* 2007; 347: 127–132.
42. Kopsaftopoulos FP and Fassois SD. Identification of stochastic systems under multiple operating conditions: the vector dependent FP-ARX parametrization. In: *Proceedings of 14th Mediterranean conference on control and automation*, Ancona, Italy, 2006.
43. Kopsaftopoulos FP and Fassois SD. Vibration-based fault detection and assessment in a scale aircraft structure via stochastic VFP-ARX models. In: *Proceedings of the 3rd European workshop on structural health monitoring (EWSHM)*, Granada, Spain, 2006.
44. Kopsaftopoulos FP, Magripis SG, Amplianitis AD, et al. Scalar and vector time series methods for vibration based damage diagnosis in an aircraft scale skeleton structure. In: *Proceedings of the ASME 2010 10th Biennial conference on engineering systems design and analysis*, Istanbul, Turkey, 2010.
45. Kopsaftopoulos FP and Fassois SD. A stochastic functional model based method for vibration based damage detection, localization, and magnitude estimation. *Mech Syst Signal Proc* 2013; 39(1–2): 143–161.
46. Kopsaftopoulos F and Fassois S. Vibration based health monitoring for a lightweight truss structure: experimental assessment of several statistical time series methods. *Mech Syst Signal Proc* 2010; 24(7): 1977–1997.
47. Kopsaftopoulos F, Nardari R, Li Y-H, et al. A stochastic global identification framework for aerospace structures operating under varying flight states. *Mech Syst Signal Proc* 2018; 98: 425–447.
48. Kopsaftopoulos FP and Fassois SD. A functional model based statistical time series method for vibration based damage detection, localization, and magnitude estimation. *Mech Syst Signal Proc* 2013; 39(1–2): 143–161.
49. Spiridonakos M and Fassois S. An FS-TAR based method for vibration-response-based fault diagnosis in stochastic time-varying structures: experimental application to a pick-and-place mechanism. *Mech Syst Signal Proc* 2013; 38(1): 206–222.
50. Spiridonakos M and Fassois S. Non-stationary random vibration modelling and analysis via functional series time-dependent ARMA (FS-TARMA) models—a critical survey. *Mech Syst Signal Proc* 2014; 47(1–2): 175–224.
51. Ahmed S, Zhou P, Zager S, et al. Local and global structural health monitoring via stochastic functional time series methods: a critical assessment and comparison. In: *AIAA AVIATION 2023 Forum*, San Diego, CA, USA, 12–16 June 2023, p. 3460.
52. Worlton D. Experimental confirmation of Lamb waves at megacycle frequencies. *J Appl Phys* 1961; 32(6): 967–971.
53. Ahmed S and Kopsaftopoulos F. Investigation of broadband high-frequency stochastic actuation for active-sensing SHM under varying temperature. In: *Proceedings of the 12th international workshop on structural health monitoring*, Stanford, CA, USA, 2017.
54. Poulimenos A and Fassois S. Parametric time-domain methods for non-stationary random vibration modelling and analysis—a critical survey and comparison. *Mech Syst Signal Proc* 2006; 20(4): 763–816.
55. Poulimenos AG and Fassois SD. Output-only stochastic identification of a time-varying structure via functional series TARMA models. *Mech Syst Signal Proc* 2009; 23(4): 1180–1204.
56. Ahmed S, Amer A, Varela CA, et al. Data-driven state awareness for fly-by-feel aerial vehicles via adaptive time series and Gaussian process regression models. In: *Dynamic data driven applications systems: Third international conference, DDDAS 2020*, Boston, MA, USA, 2–4 October 2020. Cham: Springer, pp. 57–65.
57. Conforto S and D'alessio T. Spectral analysis for non-stationary signals from mechanical measurements: a parametric approach. *Mech Syst Signal Proc* 1999; 13(3): 395–411.
58. Liporace LA. Linear estimation of nonstationary signals. *J Acoust Soc Am* 1975; 58(6): 1288–1295.
59. Fouskitakis GN and Fassois SD. On the estimation of nonstationary functional series TARMA models: an isomorphic matrix algebra based method. *J Dyn Sys Meas Control* 2001; 123(4): 601–610.
60. Kozin F and Nakajima F. The order determination problem for linear time-varying AR models. *IEEE Trans Autom Control* 1980; 25(2): 250–257.

61. Petsounis K and Fassois S. Non-stationary functional series TARMA vibration modelling and analysis in a planar manipulator. *J Sound Vibr* 2000; 231(5): 1355–1376.
62. Grenier Y. Time-dependent ARMA modeling of nonstationary signals. *IEEE Trans Acoust Speech Signal Proc* 1983; 31(4): 899–911.
63. Tsatsanis MK and Giannakis GB. Subspace methods for blind estimation of time-varying FIR channels. *IEEE Trans Signal Proc* 1997; 45(12): 3084–3093.
64. Sotiriou D, Kopsaftopoulos F and Fassois S. An adaptive time-series probabilistic framework for 4-D trajectory conformance monitoring. *IEEE Trans Intell Trans Syst* 2016; 17(6): 1606–1616.
65. Ljung L. *System identification: Theory for the user*. 2nd ed. Upper Saddle River, NJ: Prentice-Hall, 1999.
66. Akaike H. Prediction and entropy. In: Atkinson AC and Fienberg SE (eds.) *A celebration of statistics*. New York, NY: Springer, 1985, pp. 1–24.
67. Schwarz G. Estimating the dimension of a model. *Ann Statist* 1978; 6(2): 461–464.
68. Simon D. *Evolutionary optimization algorithms*. Hoboken, NJ: John Wiley & Sons, 2013.
69. Lamb H. On waves in an elastic plate. *Proc R Soc Lond A* 1917; 93(648): 114–128.
70. Kopsaftopoulos FP. *Advanced functional and sequential statistical time series methods for damage diagnosis in mechanical structures*. PhD Thesis, Department of Mechanical Engineering & Aeronautics, University of Patras, Patras, Greece, 2012.